



Radial Motions and Radial Gas Flows in Local Spiral Galaxies

Enrico M. Di Teodoro^{1,2} and J. E. G. Peek^{1,2}

¹ Department of Physics & Astronomy, Johns Hopkins University, Baltimore, MD 21218, USA; editeodoro@jhu.edu

² Space Telescope Science Institute, 3700 San Martin Drive, Baltimore, MD 21218, USA

Received 2021 July 15; revised 2021 September 17; accepted 2021 October 3; published 2021 December 23

Abstract

We determine radial velocities and mass flow rates in a sample of 54 local spiral galaxies by modeling high-resolution and high-sensitivity data of the atomic hydrogen emission line. We found that, although radial inflow motions seem to be slightly preferred over outflow motions, their magnitude is generally small. Most galaxies show radial flows of only a few km s^{-1} throughout their H I disks, either inward or outward, without any clear increase in magnitude in the outermost regions, as we would expect for continuous radial accretion. Gas mass flow rates for most galaxies are less than $1 M_{\odot} \text{ yr}^{-1}$. Over the entire sample, we estimated an average inflow rate of $0.3 M_{\odot} \text{ yr}^{-1}$ outside the optical disk and of $0.1 M_{\odot} \text{ yr}^{-1}$ in the outskirts of the H I disks. These inflow rates are about 5–10 times smaller than the average star formation rate of $1.4 M_{\odot} \text{ yr}^{-1}$. Our study suggests that there is no clear evidence for systematic radial accretion inflows that alone could feed and sustain the star formation process in the inner regions of local spiral galaxies at its current rate.

Unified Astronomy Thesaurus concepts: Disk galaxies (391); Galaxy radial velocities (616); Galaxy accretion (575); Galaxy kinematics (602); Galaxy evolution (594)

1. Introduction

Gas accretion is an important process in the evolution of galaxies. Most star-forming spiral galaxies, including our own Milky Way, are believed to have been forming stars at an almost constant, or only slightly declining, rate over cosmic time (e.g., Panter et al. 2007; Aumer & Binney 2009; Madau & Dickinson 2014). Given their average amount of gas, star-forming galaxies should deplete their entire gas content on timescales of only a few billion years (e.g., Leroy et al. 2008; Bigiel et al. 2011). To sustain their star formation rate (SFR) at a quasi-steady state for longer times, a continuous replenishment of fresh gas from the surroundings at a rate roughly equal to the SFR is needed (e.g., Fraternali & Tomasetti 2012). The need for continuous accretion of metal-poor gas is also invoked to explain the relative scarcity of low-metallicity stars in disks (G-dwarf problem; van den Bergh 1962; Worthey et al. 1996; Haywood et al. 2019).

Fresh gas can be acquired either via galaxy merging or via accretion from the circumgalactic and intergalactic media (CGM and IGM, respectively). Observational evidence suggests that, at least in the local universe, mergers cannot bring enough gas into spiral galaxies (Di Teodoro & Fraternali 2014), while direct observation of gas accretion from the CGM/IGM still remains sparse and accretion rates very uncertain (Sancisi et al. 2008; Putman et al. 2012). From a theoretical point of view, hydrodynamical simulations of galaxy formation predict that large amounts of pristine gas can be accreted onto galaxies from the IGM, either via cold gas filaments that directly feed the inner regions of a galaxy (“cold” mode) or via cooling of hot coronal gas that surrounds galactic disks (“hot” mode; e.g., Kereš et al. 2005; Nelson et al. 2013; Stern et al. 2020). According to simulations, gas accretion occurs mostly through the cold mode in low-mass galaxies and at high redshifts, while the hot mode prevails in more massive systems and at low redshift.

In the classical picture of galaxy formation, disk galaxies grow inside out over time by acquiring high angular

momentum material from the large-structure IGM (e.g., Fall & Efstathiou 1980; Pichon et al. 2011; Lagos et al. 2017; El-Badry et al. 2018). Gas infalling onto a galaxy, subject to the torques exerted by the rotating disk/halo, can settle into a corotating accretion disk that extend out to very large radii (Stewart et al. 2011, 2013). Therefore, cosmological accretion is expected to occur mostly in the outskirts of galactic disks. The presence of large corotating disks or torus-like structures of cool material has been also proposed to explain observations of the CGM in low-redshift star-forming galaxies (e.g., Ho et al. 2017; Tumlinson et al. 2017). To become available for star formation, this fresh gas needs to be transported efficiently from the outermost to the inner regions of a disk, which is where most of the star formation process occurs. In this picture, inward radial gas flows through a galactic disk are expected (e.g., Ho et al. 2019). These radial flows are also believed to play a fundamental role in the chemical evolution of galaxies, in particular in the development of abundance gradients across the disk (Lacey & Fall 1985; Goetz & Koeppen 1992; Portinari & Chiosi 2000; Mott et al. 2013, among many others), although the radial velocities needed by chemodynamical models are generally small, of the order of a few km s^{-1} only (e.g., Bilitewski & Schönrich 2012; Pezzulli & Fraternali 2016).

The atomic hydrogen (H I) emission line at 21 cm is arguably the best way to trace the outskirts of gaseous disks of local spiral galaxies and search for these alleged radial gas inflows. Atomic gas dominates at large radii and H I disks typically extend 2–3 times farther away than stellar disks. The gas surface density in the outskirts of disks is low enough that a significant radial accretion would imply detectable radial inward velocities. Moreover, H I gas often shows significant asymmetries in their outermost regions that might be a signature of ongoing or recent gas accretion (Sancisi et al. 2008) from either the IGM or from mergers. This intrinsic disturbed nature of H I disks makes it challenging to measure robustly the amount of mass that flows inward/outward. A further complication arises from the fact that radial motions can easily be an order of magnitude or more smaller than typical

rotation motions, which always dominate the overall kinematics of a disk galaxy. Therefore, extracting the radial flow signal from spectral H I data cubes is not trivial.

To date, a few studies have used H I data to investigate radial motions in small samples of galaxies (Wong et al. 2004; Trachternach et al. 2008; Schmidt et al. 2016). It is however still unclear whether radial inflows in spiral galaxies are negligible (Wong et al. 2004) or if, at least for a good fraction of galaxies, radial mass inflows can be large enough to feed and sustain the star formation (Schmidt et al. 2016). In this work, we intend to improve upon previous studies by performing a systematic search for radial flows in local disks. We put together a relatively large sample of 54 galaxies with high-quality H I archival data and, using a state-of-the-art 3D modeling technique, we accurately derive their kinematics and we quantify the velocity and amount of gas that flows radially through their disks.

The remainder of this paper is organized as follows. Section 2 introduces our galaxy sample and the data that we use in our analysis. In Section 3, we illustrate the expected signature of radial motions in a rotating disk, we describe in detail our kinematical modeling procedure, and we test its robustness. The results of our analysis are presented in Section 4. Section 5 compares our findings to previous works and discusses the limitations of our measurements and implications for gas accretion theories. Finally, we summarize and conclude in Section 6.

2. Galaxy Sample and Data

For this study, we made use of publicly available H I interferometric data of local spiral galaxies. In particular, we chose to analyze a sample of nearby galaxies observed by some of the best available H I surveys, including The H I nearby Galaxy Survey (THINGS; Walter et al. 2008), the Hydrogen Accretion in LLocal GAlaxieS survey (HALOGAS; Heald et al. 2011), the Local Volume H I Survey (LVHIS; Koribalski et al. 2018), the Westerbork survey of neutral Hydrogen in Irregular and SPiral galaxies (WHISP; van der Hulst et al. 2001), the Very Large Array (VLA) Imaging of Virgo in Atomic gas survey (VIVA; Chung et al. 2009), the ATLAS^{3D} H I survey (Serra et al. 2012) and the H I eXtreme galaxy survey (HIX; Lutz et al. 2017). Our sample was chosen on the basis of four main selection criteria: (i) rotation velocity, (ii) sensitivity of the H I data, (iii) number of resolution elements and (iv) the inclination angle. Because we aim to study radial accretion flows in star-forming disks, we select only galaxies that reach a velocity of at least 100 km s^{-1} in the flat part of their rotation curve. Measuring radial gas flows out to the outermost regions of disks requires very high quality data, having both high sensitivity and high spatial resolution. For this reason, we only select data with a H I column-density sensitivity better than $\sim 5 \times 10^{19} \text{ cm}^{-2}$, and we require that galaxies are detected with at least 15 spatial resolution elements across the major axis of the disk. Finally, to avoid problems with the derivation of galaxy kinematics, we discard high-inclined and low-inclined galaxies and we only accept disks with intermediate inclination angles i , i.e., $30^\circ \lesssim i \lesssim 80^\circ$.

Our final sample is composed of 54 well-known and well-studied spiral galaxies that we list in Appendix A. Our galaxies have distances $D \lesssim 40 \text{ kpc}$, stellar masses $9 \lesssim \log M_*/M_\odot \lesssim 11$, and morphology ranging from early-type disks (e.g., S0, Sa) to late-type disks (e.g., Sb, Sc). Galaxies inhabit a range of different

environments, from low-density environments to galaxy clusters (e.g., Virgo cluster). Twelve galaxies are from THINGS, 8 from HALOGAS, 8 from WHISP, 6 from VIVA, 5 from ATLAS^{3D}, 5 from LVHIS, 3 from HIX, while the remaining 7 are from different published studies (see Appendix A). Because we value sensitivity over spatial resolution for this study, we use natural-weighted instead of robust-weighted (Briggs 1995) data cubes whenever available (e.g., THINGS, LVHIS). For WHISP data, we use data cubes smoothed to a $30''$ spatial resolution. H I data for these galaxies have typical beam sizes $10''\text{--}100''$ and velocity channel widths of $4\text{--}8 \text{ km s}^{-1}$.

A wealth of ancillary data and measurements are available for most of these galaxies in the literature. For our purposes, we only need information on the distances and on the SFRs of our galaxies. We adopt homogenized distances and uncertainties from the Extragalactic Distance Database (EDD; Tully et al. 2009) and the CosmicFlows project (Tully et al. 2016). Star formation rates for 45 out 54 galaxies are taken from the catalog by Leroy et al. (2019), which were estimated combining data from the Wide-field Infrared Survey Explorer (WISE; Wright et al. 2010) and from the Galaxy Evolution Explorer (GALEX; Martin et al. 2005). For the remaining 9 galaxies, we estimate SFRs from WISE W3-band luminosities at $12 \mu\text{m}$, following the calibrations of Cluver et al. (2017). SFRs for our galaxies range from $0.01 M_\odot \text{ yr}^{-1}$ up to $6 M_\odot \text{ yr}^{-1}$, with average and median values over the entire sample of 1.4 and $0.9 M_\odot \text{ yr}^{-1}$, respectively. The typical uncertainty on the SFRs is 0.2 dex. Finally, all galaxies in our sample have multiband optical images from either the Sloan Digital Sky Survey (SDSS; Eisenstein et al. 2011), the Panoramic Survey Telescope and Rapid Response System survey (Pan-STARRS; Chambers et al. 2016), or the Dark Energy Spectroscopic Instrument (DESI) Legacy Surveys (Legacy, Dey et al. 2019). We use these images to determine the central coordinates of our galaxies, the size of their stellar disks, and whether the galaxies rotate clockwise or counterclockwise.

3. Methods

3.1. Radial Motions in a Rotating Disk

The first step in our analysis consists of deriving reliable radial velocities as a function of radius for our galaxies. The presence of radial motions in a galaxy modifies the emission-line profiles with respect to the case of a purely rotating disk. The geometry of a disk galaxy observed onto the plane of the sky is commonly parameterized through three quantities: (1) the center of the galaxy (x_0, y_0) , (2) the inclination angle i of the midplane of the disk with respect to the line of sight ($i = 90^\circ$ for edge-on), and (3) the position angle ϕ of the apparent major axis of the disk projected onto the sky. A particle of gas subject to both rotation and radial motions in such a system will have an observed line-of-sight velocity V_{los} given by (e.g., Begeman 1987)

$$V_{\text{los}} = V_{\text{sys}} + (V_{\text{rot}} \cos \theta + V_{\text{rad}} \sin \theta) \sin i, \quad (1)$$

where V_{sys} is the systemic velocity of the galaxy, V_{rot} is the azimuthal (rotation) velocity component, V_{rad} is the radial-velocity component, and θ is the azimuthal angle into the plane of the disk, with $\theta = 0^\circ$ corresponding to the major axis. Motions perpendicular to the plane of the disk are not considered here. From Equation (1), it is already clear that

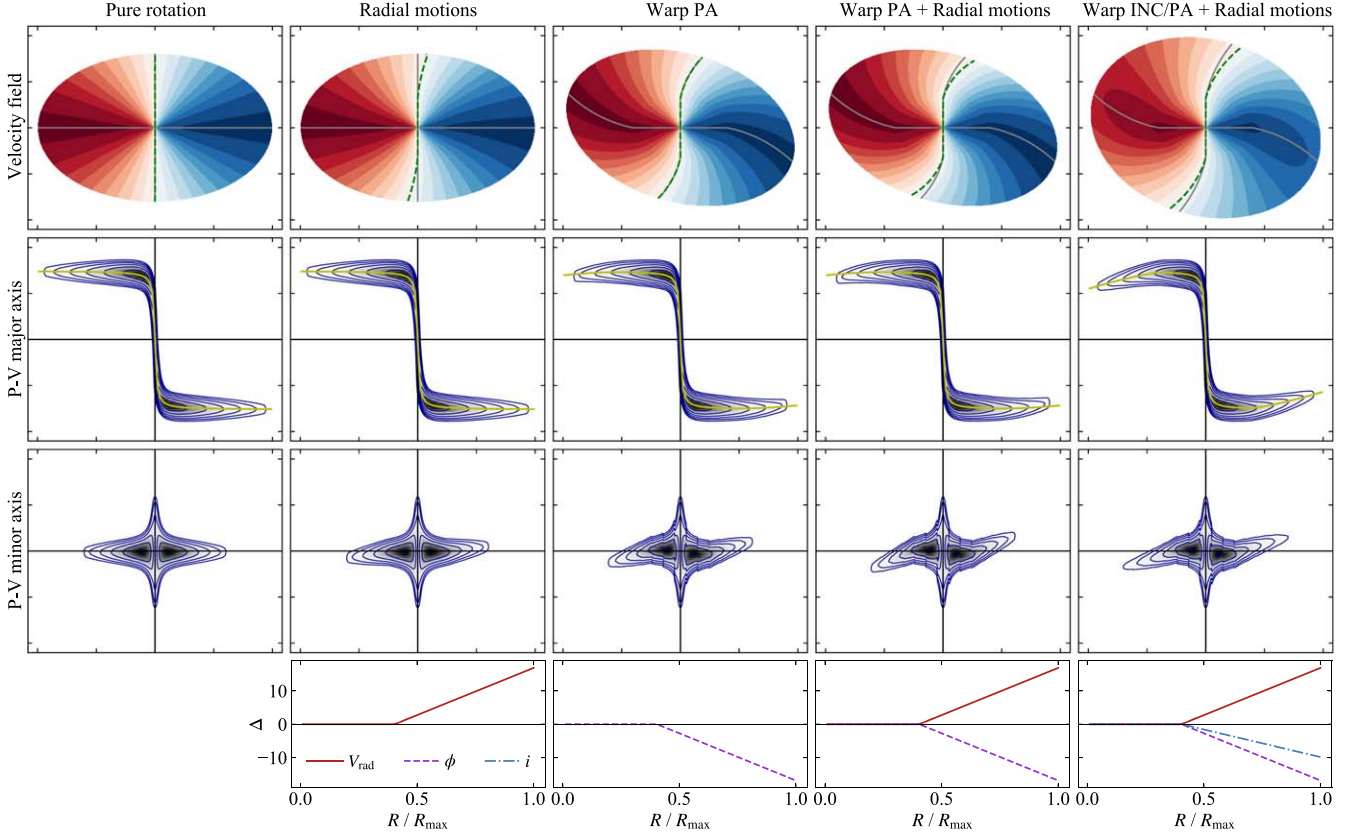


Figure 1. Toy models of a rotating disk with warps and/or radial motions. From the left to the right: (1) a purely rotating disk with a flat rotation curve, (2) a disk with radial motions in the outer regions, (3) a disk with a warp in position angle in the outer regions, (4) a disk with both radial motions and a position angle warp, and (5) a disk with radial motions and a warp in both position and inclination angle. We show the velocity field (first row), position–velocity slices along the major and minor axes (second and third rows, respectively), and the radial variations of V_{rad} (km s^{-1} , red solid line), ϕ (deg, purple dashed line), and i (deg, cyan dashed-dotted line) with respect to their initial value in each model. On the velocity fields, the major/minor axes of the disk (gray solid line) and the velocity corresponding to the systemic velocity (green dashed line) are shown. On the P-V along the major axis, we plot the V_{los} (yellow line), i.e., Equation (1) with $\theta = 0^\circ$.

rotation has a larger effect on V_{los} in the regions close to the major axis of a galaxy ($\theta \simeq 0^\circ$), while radial motions show up more prominently on the minor axis ($\theta \simeq 90^\circ$).

All above geometrical and kinematical parameters are usually not constant across a disk, but they can vary as a function of radius R . In particular, variations (warps) of the position and inclination angles, which are often observed in H I disks (e.g., Battaglia et al. 2006), can add complexity to the observed velocity structure of a galaxy. We take advantage of Figure 1 to illustrate the expected effect of radial motions and warps on an emission-line data cube of a galaxy. Each column in Figure 1 denotes a different kinematical toy model. We show a disk in pure rotation with a flat rotation curve as a reference, and the same disk with additional radial motions and/or a warp in the outer regions of the galaxy. For each model, we plot the velocity field with kinematical axes (gray) and systemic velocity (green) highlighted, and position–velocity (P-V) slices taken through the galaxy center and along the horizontal and vertical direction, representing approximately (or exactly in cases with no warp) the major and minor axes of the disk, respectively. Both radial motions and a warp in the position angle (second and third model) alone cause a clear twist of the line-of-sight velocity contours near the minor axis with respect to a pure rotating disk. However, while a warp produces an actual bending of the kinematical minor axis, resulting in an equivalent bend of the major axis as well, radial motions only introduce an offset between the systemic velocity and the

observed velocity along the minor axis and have no effect on the major axis (Equation (1)). As a consequence, when both a position angle warp and radial motions are present (fourth model), the former sets the twist of the major/minor axis, while the latter adds a further shift of the contour corresponding to the systemic velocity near the minor axis. A warp in inclination (last model) does not cause any further twist of the isovelocity contours, but only scales the magnitude of the line-of-sight velocity and changes the projected shape of the disk. The same effects are also clearly recognizable in the P-Vs along the major and minor axes. Because radial motions and warps have different effects in different regions of a disk, it is possible, although not trivial, to disentangle their relative contributions to the observed V_{los} through the kinematical model.

3.2. 3D Tilted-ring Modeling

We used a custom-modified version of the 3D kinematical software ³DBAROLO³ (BB; hereinafter Di Teodoro & Fraternali 2015) to model the kinematics of our galaxy sample and to derive radial-velocity profiles. Unlike traditional methods that mostly apply to 2D velocity fields (e.g., Begeman 1987; Spekkens & Sellwood 2007), BB simulates H I data cubes of galaxies using tilted-ring models and performs the fit directly in the 3D observational space (3DFIT

³ Code is available at <https://editeodoro.github.io/Bbarolo>. This paper uses version 1.6.1. (Di Teodoro 2021).

task). This approach exploits the full information available in 3D data sets, properly taking into account observational biases due to the finite spatial/spectral resolution of a telescope (see Di Teodoro & Fraternali 2015 for details). A galaxy model in BB is defined through four main geometrical parameters, $\mathbf{x}_{\text{geom}} = (x_0, y_0, \phi, i)$, and four kinematical parameters, $\mathbf{x}_{\text{kin}} = (V_{\text{sys}}, V_{\text{rot}}, V_{\text{rad}}, \sigma_{\text{gas}})$, where σ_{gas} is the gas intrinsic velocity dispersion. All these parameters can in theory be varied as a function of radius R . Galaxy models defined in this way are mapped into a 3D emission-line data cube, having two spatial dimensions representing the position onto the plane of the sky (x, y) and one spectral dimension representing the line-of-sight velocity V_{los} , and the parameters optimized to reproduce the observed data cubes.

We used a standardized procedure and options to model the 54 galaxies in our sample. First of all, to reduce the dimensionality of the problem, we decided to fix the center of galaxies and their systemic velocity during the fit. Because the spatial resolution of H I data is much poorer than in optical data, we assumed galaxy centers taken from z -band optical images from the SDSS/Pan-STARRS/Legacy surveys. Uncertainties associated with optical centers are less than a few arcseconds, always much smaller than the beam size in the H I data. Systemic velocities were calculated directly by BB from the global H I profiles as the midpoint between the velocities corresponding to the 20% of the peak flux, with typical errors of the order of the channel width. All others quantities ($\phi, i, V_{\text{rot}}, V_{\text{rad}}, \sigma_{\text{gas}}$) are free parameters of our models and they are fitted to the data in a set of concentric rings at increasing radii. The initial values for these parameters needed by the fitting algorithm are estimated by BB itself. Masks for the fit were built using the source-finder method, with a primary threshold of $5 \times \sigma_{\text{rms}}$ and a secondary threshold of $2 \times \sigma_{\text{rms}}$, where σ_{rms} is the rms noise of the data (see BB documentation and main paper for further details).

After extensive testing on mock observations (see Section 3.4), we determined that a three-step fit approach allowed us to recover robust radial-velocity profiles, disentangling the effect of warps and radial motions. The first two steps aim to determine the rotation curve and the warp and follow a classical tilted-ring modeling procedure: during an initial fit, radial motions are null while the geometrical and the other kinematical parameters are kept free. For the second step, the inclination and position angles are regularized to some function and only the rotation velocity and velocity dispersion are fitted. This regularization is important to avoid that numerical oscillations in the geometrical parameters translate into nonphysical discontinuities in the rotation curve. We used either a Bezier curve or a constant function to regularize the geometrical angles, depending on their degree of variation with radius after step one. In particular, we fixed i to a constant value whenever the first step returned no clear indication of a coherent warp in inclination with radius. In these two steps, we set a $(\cos \theta)^2$ weight for the fit, because the information on the rotation velocity/warp is mostly near the major axis ($\theta \approx 0^\circ$), and we excluded pixels that lie within 20° from the minor axis, which allowed us to minimize any effect of possible radial motions on the fit. During the third and final step, we only fitted for the radial velocity and we fixed all other parameters to the values previously determined. Because radial motions have a stronger effect near the minor axis ($\theta \approx 90^\circ$), this time we used a $(\sin \theta)^2$ weight and we excluded pixels within 20° from

major axis. Errors on best-fit parameters were estimated through BB's default Monte Carlo method (Di Teodoro & Fraternali 2015).

Radial velocities derived through kinematical modeling alone do not inform on whether radial motions are directed toward the center of galaxies (inflow) or toward the external regions (outflow). Knowing in which direction a galaxy rotates is required to interpret correctly the nature of measured radial motions. BB's definition of V_{rad} implies that positive (negative) velocities are outflow (inflow) motions when a galaxy is rotating clockwise, and inflow (outflow) when a galaxy is rotating counterclockwise. Because this information is not available in H I data, we used the winding of spiral arms in optical images to determine the rotation direction, under the assumption that spiral galaxies spin with their arms trailing the direction of rotation. Out of 54 galaxies in our sample, we found that 22 galaxies are rotating clockwise and 29 counterclockwise, while it was not possible to determine the rotation direction in three S0 galaxies having no prominent spiral arms (NGC 2685, NGC 3941, and NGC 5102). We used this information to correct the sign of the derived radial velocities, such that, in the remainder of the paper, $V_{\text{rad}} < 0$ always indicates inflow and $V_{\text{rad}} > 0$ outflow.

3.3. Surface-density and Mass-flow Profiles

Radial-velocity profiles $V_{\text{rad}}(R)$ obtained through 3D kinematical modeling can be combined with H I surface-density profiles $\Sigma_{\text{H I}}(R)$ to estimate H I-mass-flow-rate profiles $\dot{M}_{\text{H I}}(R)$. We derived H I intensity profiles $I(R)$ from unmasked total intensity H I maps, averaging the integrated flux along elliptical rings defined by the best-fit geometrical parameters found with the kinematical modeling (ELLPROF task in BB). The error on $I(R)$ is calculated as the standard deviation of the integrated flux in each ring. Under the assumption that the H I emission-line is optically thin, the intensity profile $I(R)$ can be easily converted to a face-on H I mass surface-density $\Sigma_{\text{H I}}(R)$ (e.g., Roberts 1975):

$$\frac{\Sigma_{\text{H I}}(R)}{[M_{\odot} \text{ pc}^{-2}]} = 8794 \frac{I(R) \cos(i(R))}{[\text{Jy beam}^{-1} \text{ km s}^{-1}]} \left(\frac{B_{\text{maj}} B_{\text{min}}}{[\text{arcsec}^2]} \right)^{-1}, \quad (2)$$

where B_{maj} and B_{min} are the full widths at half-maximum of the major and minor axes of the beam and $\cos i$ corrects for the inclination of the disk. The average radial flow of H I mass $\dot{M}_{\text{H I}}$ at a given radius R is therefore

$$\dot{M}_{\text{H I}}(R) = 2\pi R \Sigma_{\text{H I}}(R) V_{\text{rad}}(R). \quad (3)$$

The total neutral gas mass flow is $\dot{M} = 1.33 \dot{M}_{\text{H I}}$, where the factor 1.33 takes into account the primordial abundance of helium. As for the radial velocity, an $\dot{M} < 0$ indicates gas inflow (accretion) and an $\dot{M} > 0$ indicates gas outflow.

3.4. Tests on Mock Observations

To validate the methodology described in previous sections, we tested it with a sample of synthetic H I data cubes. We simulated a set of 100 galaxies, having different geometrical and kinematical properties (GALMOD task in BB). In particular, we explored a wide range of parameters representative of real spiral galaxies: (1) different rotation curves, including slowly rising or steeply rising and flat rotation curves; (2) different H I surface-density profiles; (3) different warps in the outer regions of the disk, allowing a linear or quadratic variation of up to 20°

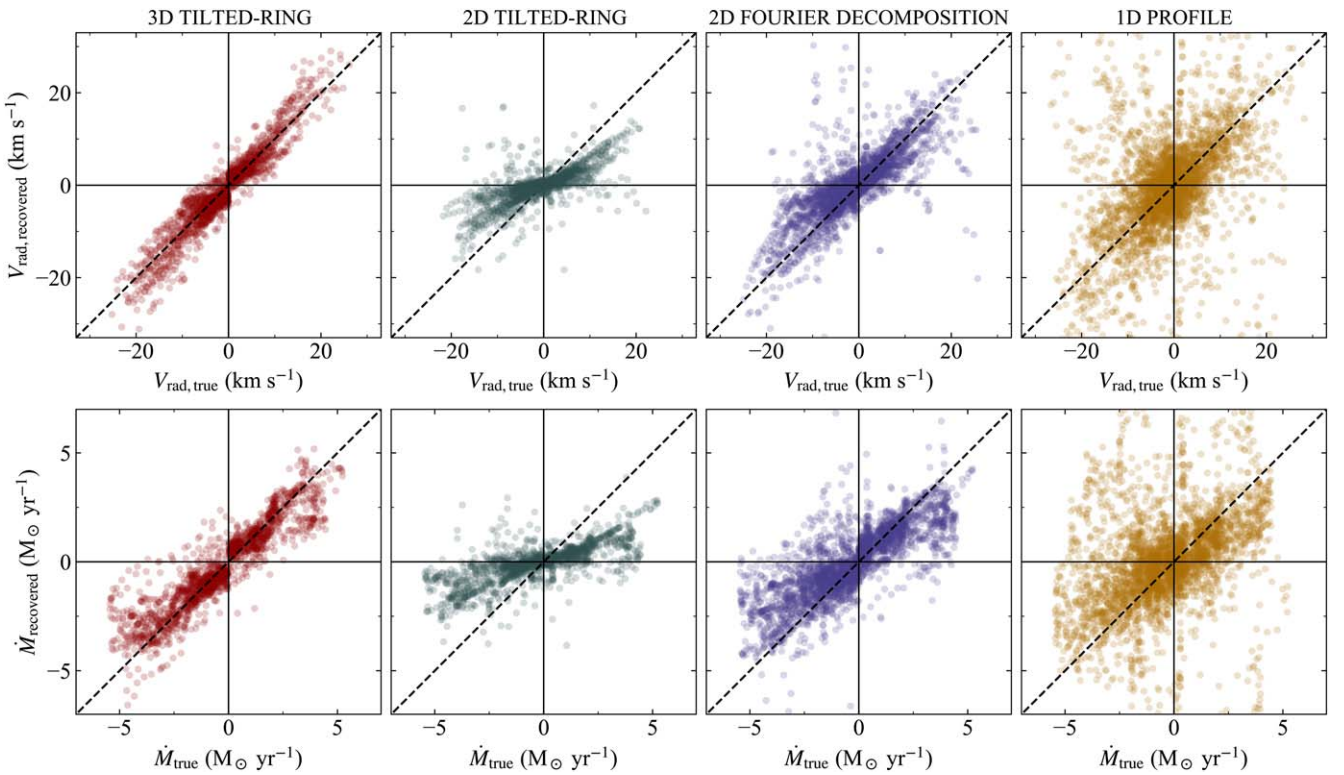


Figure 2. Comparison between four different methods to derive radial velocities (top) and mass flows (bottom) in simulated disk galaxies. In red, the 3D modeling method used in this paper (Section 3.2); in green and blue, a classical 2D tilted-ring model (Begeman 1987) and a Fourier decomposition technique (Schmidt et al. 2016) applied to the velocity field, respectively; in gold, the average 1D profile along the minor axis.

for the position angle and up to 10° for the inclination angle (always in the range $30^\circ \lesssim i \lesssim 80^\circ$); (4) different radial inflow/outflow motions both in the inner and outer disk; (5) different disk thicknesses plus the possible presence of flares in the outer H I disk. These galaxy models were mapped into mock data cubes having observational properties, in particular spatial/spectral resolutions and levels of noise, similar to those of our H I data sample. The main goal was to investigate to what extent a range of galaxy intrinsic features and of observational properties can hamper our ability to recover radial velocities and radial mass flow rates in disk galaxies.

Our 3D kinematical modeling was performed on these 100 data cubes of simulated galaxies. For comparison, we also analyzed these data sets and derived radial-velocity profiles with a classical 2D tilted-ring model (2DFIT task in BB), with a Fourier decomposition scheme of the velocity field (first moment) akin to that of Schmidt et al. (2016), and with a simple estimate of V_{rad} through Equation (1) from the averaged 1D V_{los} profile in the P-V along the minor axis. Surface-density profiles were always derived as described in Section 3.3. Figure 2 shows plots of the “true” versus recovered values of V_{rad} (top panels) and \dot{M} (bottom) with these four methods. Each point in the plots denotes a measurement in a single ring. It is clear that both a simple 2D tilted-ring modeling (green) and a 1D method (gold) are unsuitable to derive robust radial motions and mass flows, the former showing a strong bias toward lower radial flows and the latter returning very inaccurate values, mostly due to the unaccounted presence of warps. Instead, both our 3D modeling procedure (red) and the 2D Fourier decomposition of the velocity fields (blue) recover values of V_{rad} and \dot{M} more consistent with the inputs. However, the 2D method has a larger scatter and still shows some bias

toward lower radial flows, likely due to the fact that the values of V_{los} on a velocity field may not be representative of the motions in the disk plane in the presence of strong warps or thick disks. Our 3D method does not seem to produce any significant bias and recovered data points have a relatively small scatter of 3 km s^{-1} in radial velocity and of $0.5 M_\odot \text{ yr}^{-1}$ in mass flow with respect to the one-to-one relation. This suggests that our 3D modeling procedure can be safely applied to a wide range of disk galaxies with different intrinsic and observational properties.

4. Results

4.1. Radial Flows in Local Galaxies

We used our 3D procedure to carefully model the kinematics of our 54 galaxies. Each best-fit model was visually inspected and compared to the data to double-check the goodness of the fit. In a few difficult cases, initial parameters and options for the code were manually fine-tuned to attain a better fitting model. Figures 3 and 4 illustrate two examples of our 3D modeling applied to the galaxies NGC 3198 and NGC 5055 from the HALOGAS survey. A comparison between the data and our best-fit model is shown in the top panels by means of velocity fields (left) and P-V diagrams taken along the major and minor axes (right). P-Vs in particular highlight how our models (red contours) are able to reproduce almost entirely the H I emission in the data (blue contours). Bottom panels in Figures 3 and 4 show the most important model parameters derived through the modeling: the rotation curve and surface-density profile (left), the geometrical inclination and position angles (middle), and the radial velocity and gas mass-flow-rate profile (right). Similar plots of best-fit parameters for all galaxies in our sample can be

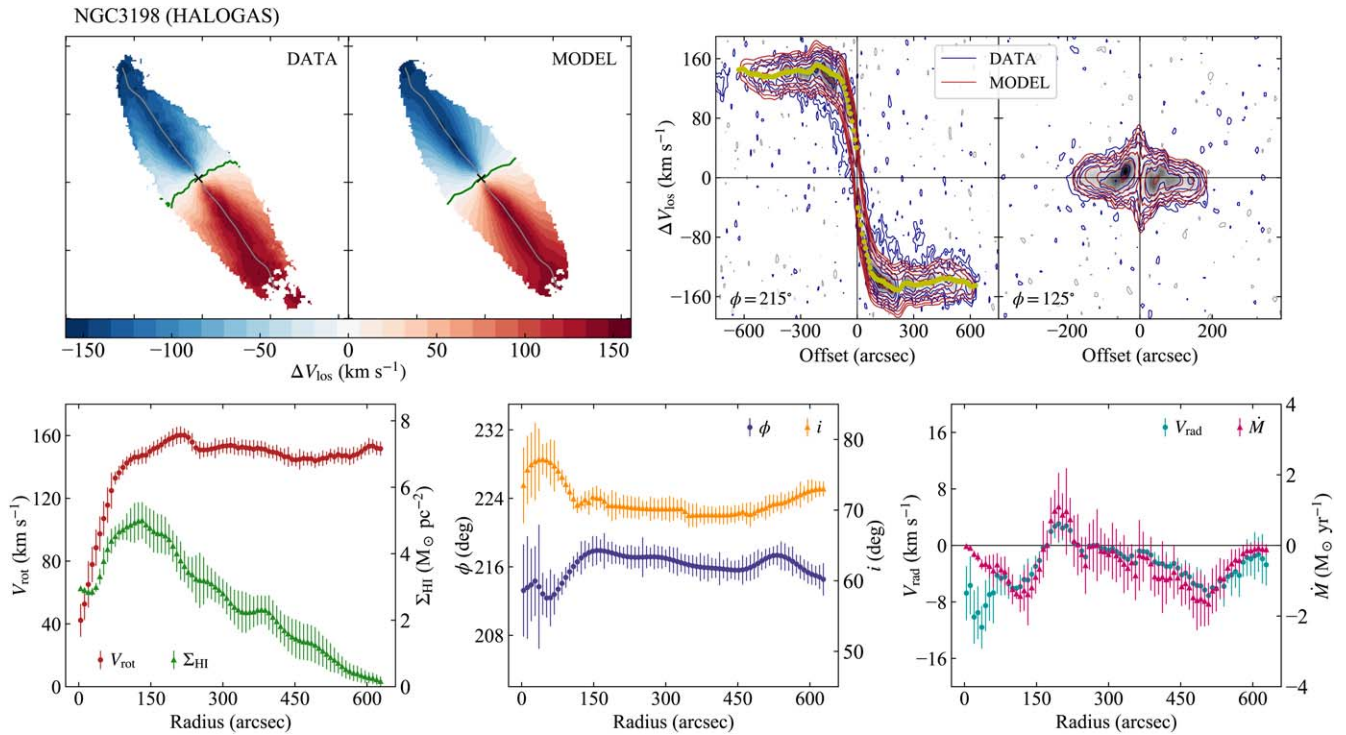


Figure 3. 3D tilted-ring modeling of the galaxy NGC 3198. Top panels: on the left, velocity fields of the data and of the best-fit model. The black crosses denote the galaxy center, the green thick lines the systemic velocity, and the gray thin lines the galaxy major axis. On the right, P-Vs slice through the average major and minor axes. Data and model are shown in blue and red contours, respectively (levels at $2^n \times \sigma_{\text{rms}}$, with $n = 0 \dots 5$). Bottom panels: derived morphokinematical parameters. Left panel shows the rotation curve (red circles) and the H I surface density (green triangles), middle panel shows the position angle (orange circles) and the inclination (blue triangles), and right panel shows the radial velocity (cyan circles) and mass flow rate (fuchsia triangles).

found in Appendix B. NGC 3198 is a fairly well-behaved spiral galaxy, with a regularly rotating H I disk out to the outermost radii, showing no signs of a warp or of a disturbed disk (ϕ and i are almost constant with radius). By contrast, NGC 5055 has one of the most extreme and warped H I disks in the local universe, with variations in ϕ and i larger than 20° and 10° , respectively. Although these two galaxies have such different H I disks, both of them only have moderate radial gas flows throughout their disk: typical radial velocities are $|V_{\text{rad}}| \lesssim 10 \text{ km s}^{-1}$, a small fraction of the rotation velocity ($|V_{\text{rot}}/V_{\text{rad}}| \gtrsim 10$). The corresponding mass flow rates are mostly $|\dot{M}| \lesssim 1 M_{\odot} \text{ yr}^{-1}$. More interestingly, these radial flows do not seem to be coherent across the entire disk. Some regions show some clear gas inflow, for example, around $R \simeq 500''$ in NGC 3198, while in other regions the gas flows outward, for example around $R \simeq 300''$ in NGC 5055 or $R \simeq 150''$ in NGC 3198.

Similar radial flows are detected in the majority of our 54 galaxies. Local and global noncircular motions in a galactic disk can be induced by a variety of physical processes, like accretion of gas with different angular momenta, viscosity in the gas layer, gas streaming along a bar, spiral arms, and, more in general, any perturbation of the gravitational potential (e.g., Lacey & Fall 1985; Thon & Meusinger 1998; Armillotta et al. 2019, 2020; Martinez-Medina et al. 2020). In general, it is not trivial to associate unambiguously measured radial flows with one or more of these processes. However, we note that some of the largest radial motions in our sample are found in the inner regions of the disks and are sometimes associated with the presence of a prominent bar (e.g., NGC 3351 or NGC 4725) or of strong spiral arms (e.g., NGC 3031 or NGC 3992).

Figure 5 summarizes radial-velocity profiles (top) and mass-flow-rate profiles (bottom) for our sample. Radii are normalized

to the radius R_{25} corresponding to the 25 mag arcsec $^{-2}$ isophote in the z band. R_{25} can be considered as the size of the optical disk where most star formation is occurring. Our galaxies typically have H I disks that extend up to $2 - 3R_{25}$. Profiles in Figure 5 are akin to those of NGC 3198 and NGC 5055: all galaxies show some degree of radial gas flows, with radial velocities typically of a few km s^{-1} , but these flows do not seem to have a preferential direction. As a consequence, the average radial velocity and mass flow rate across the sample at a given R/R_{25} are nearly constant and close to zero (red thick line). Histograms in Figure 5 show the frequency distributions of measured radial velocity and mass flow rate. We plot distributions for all radii (blue), for radii past the optical disk ($R > R_{25}$, red), and for the very outskirts of H I disks (orange), i.e., $R > R_{\text{HI}}$ where R_{HI} is the radius at which the H I surface density drops below $1 M_{\odot} \text{ pc}^{-2}$ ($R_{\text{HI}} > R_{25}$ for all galaxies in our sample with disks more extended than R_{HI}). The mean of these distributions is nearly zero (slightly negative), in both V_{rad} and \dot{M} , with no sign of a shift toward larger flows as we move toward the outer parts of galaxy disks. Therefore, we conclude that spiral galaxies in the local universe do not seem to have any systematic radial gas inflow/outflow in their outer disks.

4.2. \dot{M} versus SFR

In Figure 6 we compare the average mass flow rates \dot{M} measured in this work with the SFRs of our galaxies. Left and right panels refer to \dot{M} averaged over radii larger than the optical radius R_{25} and over radii larger than the H I radius R_{HI} , respectively. We note that 11 galaxies in our sample that do not reach $\Sigma_{\text{HI}} < 1 M_{\odot} \text{ pc}^{-2}$ are removed from the right plot. Blue

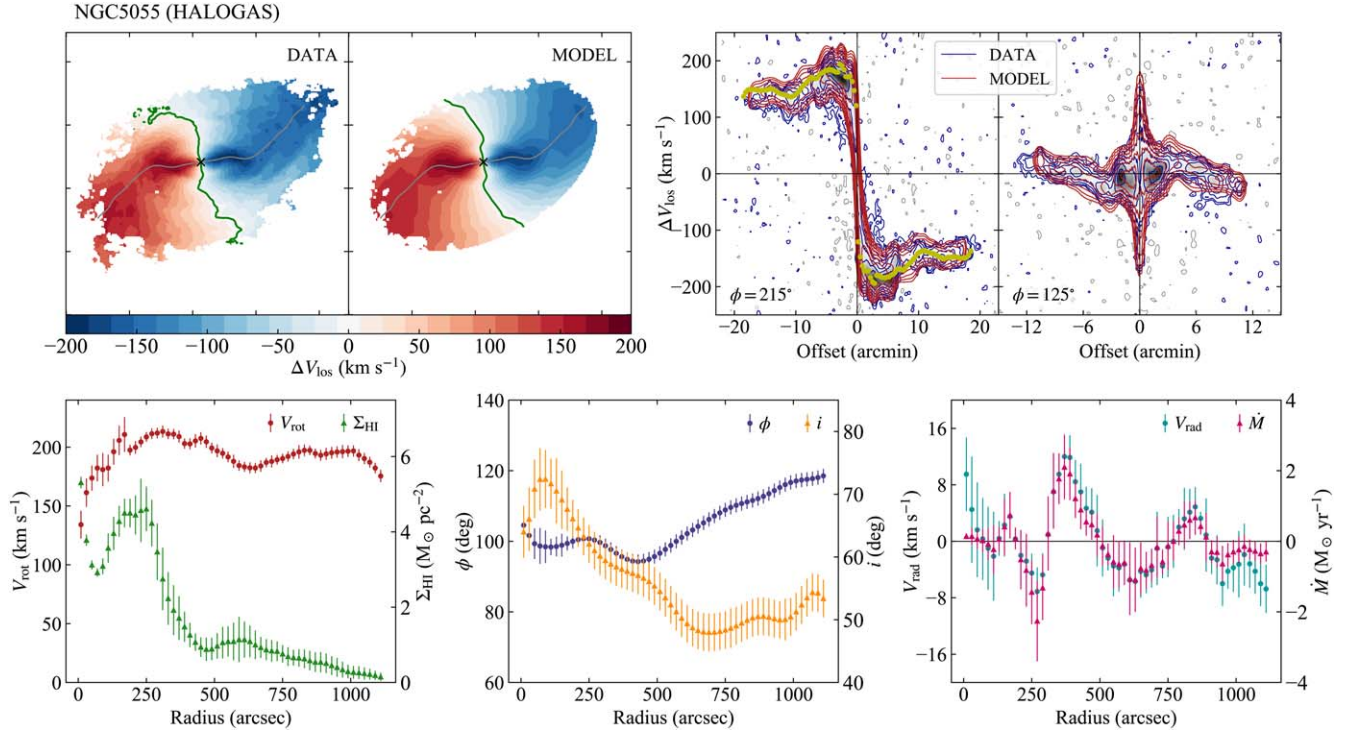


Figure 4. Same as Figure 3, but for the warped galaxy NGC 5055.

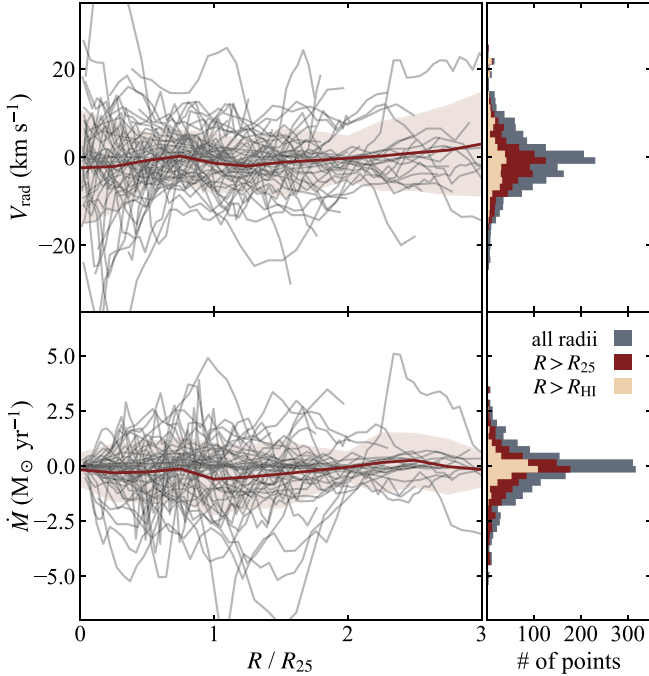


Figure 5. Gas flow radial profiles for the 54 galaxies analyzed in this work. Radial velocities and gas mass flow rates are shown in the top and bottom panels, respectively. The red thick line and shadow region denote the average and standard deviation across the entire sample. Negative (positive) values mean inflow (outflow). Histograms on the left show the corresponding distributions for all radii (blue), radii larger than the optical radius R_{25} (red), and radii larger than R_{HI} (orange).

regions in the plots mean outward flows. We highlight in red the regions where there is some inflow, but lower than the SFR, while yellow regions are where the average inflow is larger than the SFR. About half of the galaxies in our sample show

some inflow in their outer disks (negative \dot{M}), but for most of them the inflow rate is much smaller than the SFR. Eleven galaxies have inflows outside R_{25} larger than the total SFR in the stellar disk, although only three at a significance level $>1\sigma$. This number reduces to three galaxies (two at $>1\sigma$) when we average over the outermost parts of the H I disk ($R > R_{\text{HI}}$). Some of the galaxies with the largest measured gas flows, either inflows or outflows, show signs of ongoing or recent tidal encounters (e.g., NGC 5033, NGC 3621, and NGC 4651).

The mean mass flow rate over the entire sample is $-0.3 \pm 0.9 M_{\odot} \text{ yr}^{-1}$ (median $-0.1 M_{\odot} \text{ yr}^{-1}$) for $R > R_{25}$ and $-0.1 \pm 0.7 M_{\odot} \text{ yr}^{-1}$ (median $-0.1 M_{\odot} \text{ yr}^{-1}$) for $R > R_{\text{HI}}$. If we only consider galaxies with inflows, the mean mass flow rate is $-0.8 \pm 0.8 M_{\odot} \text{ yr}^{-1}$ (median $-0.4 M_{\odot} \text{ yr}^{-1}$) for $R > R_{25}$ and $-0.6 \pm 0.7 M_{\odot} \text{ yr}^{-1}$ (median $-0.3 M_{\odot} \text{ yr}^{-1}$) for $R > R_{\text{HI}}$. These values are at least a factor of 2 smaller than the average SFR of $\simeq 1.4 M_{\odot} \text{ yr}^{-1}$ of our galaxy sample. In conclusion, although our data suggest a slight preference for inflow over outflow motions, the amount of cold gas accreted alone seems insufficient to feed the star formation occurring in the stellar disk of most local spiral galaxies. Average radial velocities and mass flow rates derived in this work for all galaxies can be found in Appendix A.

5. Discussion

5.1. Caveats

Radial motions are notoriously difficult to measure in galaxies (e.g., Wong et al. 2004). Although we used a state-of-the-art 3D technique to derive galaxy kinematics and radial motions, our approach still relies on a number of assumptions and approximations that might not be always fully appropriate for real galaxies. First, our models are always symmetric both in the gas distribution and in the kinematics, while real H I disks are known to show all sort of asymmetries, like spiral

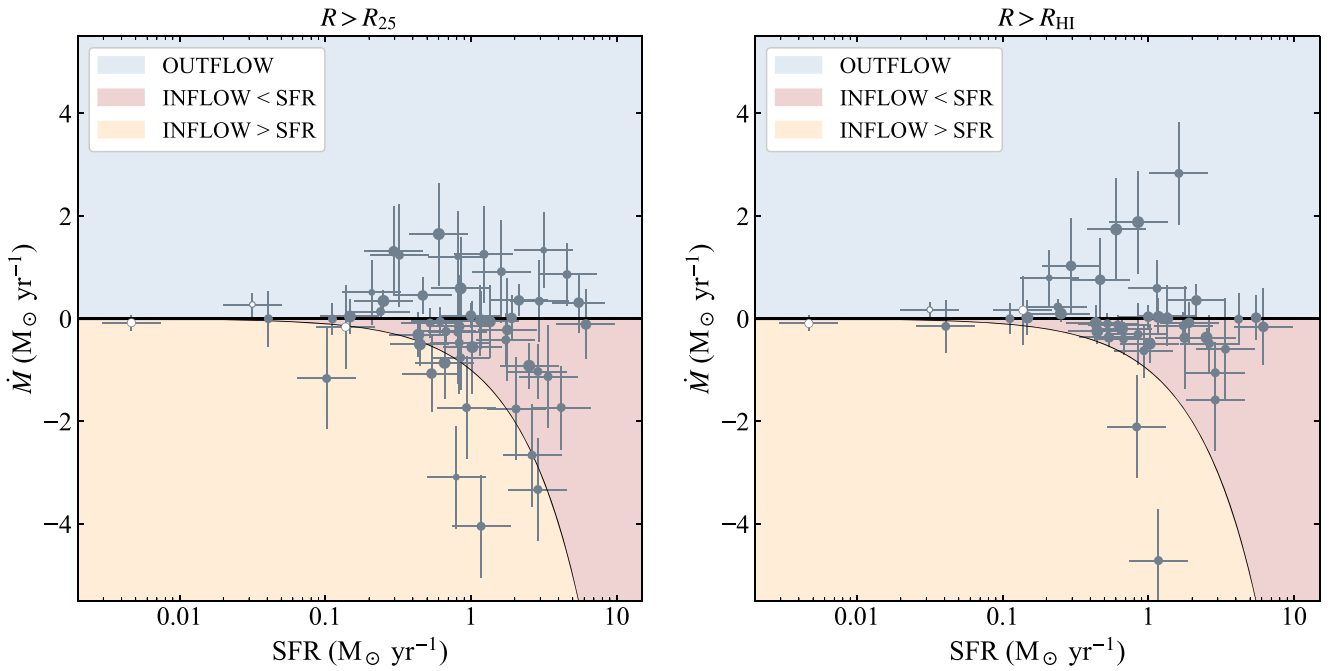


Figure 6. Comparison between average mass flow rates $\langle \dot{M} \rangle$ and star formation rates SFRs for our 54 galaxies. The average $\langle \dot{M} \rangle$ is calculated for $R > R_{25}$ (left) and for $R > R_{\text{HI}}$ (right). We indicate in blue the region where $\dot{M} > 0$, in red the region where $\dot{M} < 0$ and $|\dot{M}| < \text{SFR}$, and in yellow the region where $\dot{M} < 0$ and $|\dot{M}| > \text{SFR}$. The size of points is proportional to the goodness of the best-fit kinematical model, with bigger points indicating more robust models. The three white points denote the three galaxies for which we could not infer the rotation direction and for which $\langle \dot{M} \rangle$ might have an opposite sign.

arms, asymmetric warps, and morphological/kinematical lopsidedness (Sancisi et al. 2008), especially in the outer regions. A few galaxies in our sample also show some tidal interactions with nearby dwarf galaxies, causing further asymmetries. Our method, which fits all quantities in symmetric rings, tends to smooth out these asymmetries and to find average values that can reproduce the bulk of the gas in a ring.

A second limitation comes from the assumption that gas always moves in circular orbits. This approximation holds for the inner regions of HI disks, but it probably breaks for warped orbits as they move away from the midplane. This would affect both the rotation velocity and the radial velocity that we estimated with our 3D modeling. Finally, we also assumed that HI disks have a constant scale height and that there are no significant vertical motions. However, HI disks are expected to flare in the outermost regions (e.g., Kalberla & Dedes 2008), where the gravitational potential of the disk becomes weaker. Some vertical motions, likely of a magnitude similar to the measured radial motions, are also expected because, for example, of star formation feedback in the disk. Parameters that might be affected by an accounted for presence of flares and vertical motions include the galaxy inclination and the rotation/radial velocity.

Given the above, the magnitude of radial inflow/outflow measured in this paper for individual galaxies should be regarded as significantly uncertain. However, we do not expect the above assumptions to produce a bias in the measured radial flows over a statistical sample, but only to increase the scatter of our measurements. For example, if all galaxies in our sample were experiencing systematic and strong radial inflows in their outermost regions, this would produce a detectable effect when

averaging over the entire population, despite all the approximations in our modeling approach.

5.2. Comparison with Previous Studies

Only few former works have tried to quantify radial gas flows in HI data of local galaxies (Wong et al. 2004; Trachternach et al. 2008; Schmidt et al. 2016). While we performed a full 3D modeling of HI data cubes, all previous studies derived radial motions through a harmonic decomposition of the 2D velocity field (see the blue dots in Figure 2). Wong et al. (2004) attempted the first systematic investigation of radial gas flows in seven nearby spirals, three of which are included in our sample as well (NGCs 4414, 5033, and 5055), mostly focusing on the inner regions of the disks. Using both HI and CO data, they concluded that there is no unequivocal evidence for significant radial inflows and that most noncircular motions are attributable to the presence of bars and spiral structures. Trachternach et al. (2008) studied the effect of noncircular motions on the dark matter halo by analyzing a sample of 19 galaxies from the THINGS survey, including both spiral and dwarf galaxies (12 in common with our study). They also found that, on average, noncircular motions are smaller than $\sim 10 \text{ km s}^{-1}$ and only a small fraction of the rotation velocity ($\sim 5\%$). Therefore, our findings on a larger sample of 54 galaxies are in good agreement with both Wong et al. (2004) and Trachternach et al. (2008), i.e., we confirm that, in general, significant radial motions are not detected in local spiral galaxies.

The most recent observational study on radial gas flows is that of Schmidt et al. (2016). They reanalyzed 10 galaxies from the THINGS survey using a more sophisticated Fourier decomposition technique of the velocity field and compared the derived mass flow rates with star formation rate profiles.

Nine of these galaxies are also included in our sample (all but NGC 925). Schmidt et al. (2016) claimed that, in at least 5 out of 10 galaxies (NGCs 2403, 3198, 2903, 6946, and 7331), average mass inflow rates outside the optical disks are quite larger than the star formation rates. For the remaining five galaxies, the picture looks more complicated, showing either inflow, outward motions, or complex kinematic signatures. We note that the shape of radial profiles showed in Schmidt et al. (2016) are overall in good agreement with ours (see Appendix B), and the magnitude of their derived radial velocities are also generally within a few km s^{-1} from those measured in our work. However, their mass flow rates are consistently larger than ours. We argue that this discrepancy might be ascribable to the different masking used for the derivation of H I column densities. While we used unmasked total H I maps, Schmidt et al. (2016) relied on THINGS zeroth-moment maps, obtained with a quite aggressive masking (Walter et al. 2008). According to our tests with mock data, this type of masking may cause an overestimation of the H I column density in the faint outskirts of disks, because noisy pixels with positive values may be included in the mask without their negative counterparts. In particular, we found that this effect can be important with THINGS data, where the properties of the noise are strongly uneven across the field of view.

5.3. No Significant Radial Accretion?

Theories of galaxy evolution predict that cosmological gas is first accreted onto galaxies at large radii and then radially moves toward the inner disk to feed the star formation process (Stewart et al. 2013; Ho et al. 2019). A few recent works have studied radial gas accretion in Milky Way-like galaxies in cosmological hydrodynamical simulation (Nuza et al. 2019; Okalidis et al. 2021; Trapp et al. 2021). These studies found that the expected gas inflow radial motions in most star-forming galaxies are of the order of a few km s^{-1} within the inner optical disk and can reach 10–15 km s^{-1} in the outskirts. Predicted mass flows are of the order of a few $M_{\odot} \text{ yr}^{-1}$, usually sufficient to sustain the star formation for long times.

From our analysis, a more complex picture arises. First of all, only half of the galaxies in our sample show some radial gas inflows, suggesting that radial accretion is present in only a fraction of star-forming disks. For most of these galaxies, we measured radial velocities of a few up to about 10 km s^{-1} , in agreement with expectations from simulations, but without observing the predicted increment in the outer regions of the H I disks. Moreover, we found that radial motions are highly variable and can easily transition from inflow to outflow throughout the disk, likely due to local perturbing structures like spiral arms or bars. Although the measured amount of gas radially accreted can contribute to sustain the current star formation rate in some galaxies, it seems insufficient to support it entirely in most of them. In fact, only 2–3 galaxies in our sample have $\dot{M} > \text{SFR}$ at a $>1\sigma$ level, while most galaxies seem to have little or no radial accretion. However, we also stress that the current SFR of a galaxy and the current gas inflow rate may not be easily related to each other, as gas accretion and star formation act on different timescales. Observed gas inflowing from the external regions of the disk with typical velocities of a few km s^{-1} will be available for star formation in the inner regions on timescales $\gtrsim 1$ Gyr. Star formation and accretion rates are directly comparable only if

we assume a quasi-steady-state evolution over the past few Gyr.

Our study suggests that the observed amount of gas radially inflowing from the intergalactic and circumgalactic media at the edges of most local spiral galaxies will not be enough to sustain star formation at its current rate in the near future. This implies that either the SFR in most spiral galaxies will be declining over time or that other dominant forms of gas accretion, not requiring significant radial inflows, might be present. For example, some gas might be falling down nearly vertically onto the inner star-forming disk. We know that both the Milky Way (e.g., Wakker & van Woerden 1997; Putman et al. 2012) and M31 and M33 (e.g., Westmeier et al. 2005; Kerp et al. 2016) are surrounded by several massive H I structures (“high-velocity clouds”) residing within their inner halos, which is likely a common feature of most spiral galaxies. However, estimates of accretion rates from these H I structures are relatively small (Sancisi et al. 2008; Putman et al. 2012). A significant reservoir of fresh cold/warm gas might come from the extended and diffuse CGM observed in absorption out to ~ 150 kpc in many star-forming galaxies (Tumlinson et al. 2017), but the mode of a possible accretion of this gas is still poorly understood. Another intriguing scenario, compatible with no significant radial inflow motions, proposes that most accretion might happen at the disk–halo interface through the condensation of the hot corona triggered by supernova feedback (Marinacci et al. 2010; Armillotta et al. 2016). All these mechanisms may be working together to bring enough fresh gas into star-forming disks. Finally, another possibility is that radial accretion is an episodic and fast rather than a continuous process, triggered for example by tidal encounters and/or disk instabilities. In any case, our results seem to discourage a dominant, secular, radial accretion scenario, where most fresh gas from the CGM/IGM is steadily transported inward from the outermost to the innermost regions of disks.

6. Summary and Conclusions

In this work, we used the best H I data currently available to determine radial motions and radial gas flows in local spiral galaxies. We developed a multistep 3D technique to break the degeneracy between warps and radial motions and we derived accurate kinematical models and H I surface-density profiles for 54 nearby spiral galaxies. For most galaxies, we found radial velocities, directed either inward (inflow) or outward (outflow), of only a few km s^{-1} , without any clear increase moving toward the outermost regions of H I disks. These radial velocities translate into cold gas mass inflow/outflow rates of only a few tenths of $M_{\odot} \text{ yr}^{-1}$ in most cases. The largest radial flows are generally associated with structures like bars and spiral arms in the inner disks, and with tidal interactions and/or minor mergers in the outer disks. When averaging over the entire sample, inflow motions seem slightly favored over outflow motions, but, in general, we did not find any kinematical signature for systematic radial inflows in spiral galaxies in the nearby universe.

Instantaneous star formation rates of our galaxies were compared with the average gas mass flow rates outside the optical radius ($R > R_{25}$) and in the outermost portions of the H I disks ($R > R_{\text{HI}}$). About half of the galaxies in our sample show some degree of inflow, but only a few of them have measured mass inflow rates that could significantly sustain the star

formation process in the inner disk. We calculated a mean mass flow rate for the entire sample of $-0.3 \pm 0.9 M_{\odot} \text{ yr}^{-1}$ for $R > R_{25}$ and of $-0.1 \pm 0.7 M_{\odot} \text{ yr}^{-1}$ for $R > R_{\text{HI}}$. These mass flow rates are several times smaller than the average star formation rate of $1.4 M_{\odot} \text{ yr}^{-1}$. We conclude that, despite the uncertainties in our measurements, we do not see any convincing evidence for a secular radial gas accretion process from the IGM/CGM onto star-forming galaxies in the local universe. In most galaxies, additional channels of accretion that do not require a significant radial transport of mass in the gaseous disk are needed to feed and sustain the star formation process over the next few Gyr.

We thank F. Fraternali, N. Sanchez and S. Loebman for fruitful discussions on the topics of this paper. E.D.T. was supported by the US National Science Foundation under grant 1616177.

Facilities: VLA, WSRT, ATCA.

Software: ^{3D}BAROLO (Di Teodoro & Fraternali 2015; Di Teodoro 2021), CASA (Raba et al. 2020), ASTROPY (Astropy Collaboration et al. 2018).

Appendix A Properties of Galaxy Sample

This appendix contains a table with the sample of 54 galaxies analyzed in this work and their derived properties (Table 1). Columns are as follows: (1) Galaxy name. (2) Distances from EDD database (Tully et al. 2016). (3) Inclination angle derived with kinematic modeling. (4) Star formation rates taken from Leroy et al. (2019) or calculated from WISE W3-band luminosities. (5) Direction of rotation: A = counterclockwise, C = clockwise, ? = undefined. (6) Average radial velocity for $R > R_{25}$. Negative/positive values indicate inflow/outflow. (7) Average radial velocity for $R > R_{\text{HI}}$. Eleven galaxies do not reach $R > R_{\text{HI}}$. (8) Average gas mass flow rate for $R > R_{25}$. Negative/positive values indicate inflow/outflow. (9) Average gas mass flow rate for $R > R_{\text{HI}}$. (10) HI data cubes from: 1 = THINGS (Walter et al. 2008), 2 = HALOGAS (Heald et al. 2011), 3 = VIVA (Chung et al. 2009), 4 = WHISP (van der Hulst et al. 2001), 5 = Richards et al. (2016), 6 = LVHIS (Koribalski et al. 2018), 7 = HIX (Lutz et al. 2017), 8 = ATLAS^{3D} HI (Serra et al. 2012), 9 = Braun et al. (2009).

Table 1
Galaxy Sample Analyzed in This Work

Name	D (Mpc)	i (deg)	SFR (M_{\odot} yr $^{-1}$)	RD	$\langle V_{\text{rad},25} \rangle$ (km s $^{-1}$)	$\langle V_{\text{rad},H} \rangle$ (km s $^{-1}$)	$\langle \dot{M}_{25} \rangle$ (M_{\odot} yr $^{-1}$)	$\langle \dot{M}_{\text{HI}} \rangle$ (M_{\odot} yr $^{-1}$)	References
(1)	(2)	(3)	(4)	(5)	(6)	(7)	(8)	(9)	(10)
ESO097-G013	4.2 ± 0.7	55	5.50 ± 2.28	A	$+2 \pm 3$	$+0 \pm 3$	$+0.31 \pm 0.58$	$+0.02 \pm 0.43$	6
NGC 0210	20.9 ± 2.7	52	0.32 ± 0.15	C	$+4 \pm 4$...	$+1.24 \pm 1.48$...	8
NGC 0224	0.77 ± 0.04	77	2.51 ± 1.16	A	-6 ± 3	-7 ± 4	-0.92 ± 0.44	-0.37 ± 0.19	9
NGC 0253	3.6 ± 0.3	80	4.57 ± 2.11	C	$+5 \pm 3$...	$+0.86 \pm 0.60$...	6
NGC 0289	23.3 ± 3.2	45	1.17 ± 0.54	A	-4 ± 3	-16 ± 4	-4.05 ± 1.50	-4.71 ± 1.50	7
NGC 0949	10.3 ± 1.3	68	0.24 ± 0.11	C	$+4 \pm 3$	$+7 \pm 3$	$+0.14 \pm 0.15$	$+0.23 \pm 0.15$	2
NGC 1003	9.9 ± 2.7	79	0.21 ± 0.10	A	$+4 \pm 3$	$+7 \pm 3$	$+0.51 \pm 0.63$	$+0.79 \pm 0.55$	2
NGC 1313	4.2 ± 0.4	44	0.68 ± 0.31	C	-8 ± 3	-13 ± 4	-0.25 ± 0.25	-0.40 ± 0.31	6
NGC 2403	3.2 ± 0.3	60	0.45 ± 0.21	C	-3 ± 3	-3 ± 3	-0.50 ± 0.41	-0.25 ± 0.24	2
NGC 2685	37.8 ± 3.9	61	0.14 ± 0.06	?	$+0 \pm 3$	$+2 \pm 5$	-0.16 ± 0.81	$+0.16 \pm 0.67$	8
NGC 2841	14.1 ± 1.9	71	0.85 ± 0.39	A	$+9 \pm 3$	$+21 \pm 3$	$+0.59 \pm 1.25$	$+1.88 \pm 1.50$	1
NGC 2903	8.9 ± 1.3	66	0.44 ± 0.20	A	-3 ± 3	-3 ± 3	-0.32 ± 0.43	-0.08 ± 0.34	1
NGC 2985	16.6 ± 3.6	50	0.81 ± 0.37	C	-1 ± 3	...	-0.26 ± 1.04	...	4
NGC 3001	26.7 ± 7.4	53	1.78 ± 0.82	A	-3 ± 4	-6 ± 4	-0.22 ± 1.15	-0.37 ± 1.21	7
NGC 3031	3.7 ± 0.3	63	0.54 ± 0.25	A	-5 ± 3	-22 ± 5	-1.07 ± 0.75	-0.36 ± 0.19	1
NGC 3184	13.0 ± 1.6	24	1.35 ± 0.62	C	$+0 \pm 3$	$+2 \pm 4$	-0.18 ± 0.71	$+0.11 \pm 0.35$	1
NGC 3198	13.8 ± 1.1	73	1.02 ± 0.47	A	-2 ± 3	-4 ± 4	-0.55 ± 0.90	-0.49 ± 0.38	2
NGC 3344	10.0 ± 1.3	29	0.83 ± 0.38	C	$+0 \pm 3$...	-0.15 ± 1.10	...	4
NGC 3351	10.5 ± 0.8	45	1.17 ± 0.54	A	$+0 \pm 3$	$+1 \pm 4$	-0.03 ± 0.56	$+0.03 \pm 0.36$	1
NGC 3486	12.7 ± 2.8	45	1.15 ± 0.53	A	$+1 \pm 3$	$+6 \pm 5$	-0.04 ± 0.69	$+0.59 \pm 0.55$	5
NGC 3521	13.2 ± 3.1	70	2.63 ± 1.21	A	-7 ± 3	-6 ± 3	-2.66 ± 1.35	-0.49 ± 0.48	1
NGC 3556	9.6 ± 1.3	78	1.23 ± 0.57	C	$+6 \pm 4$...	$+1.25 \pm 0.94$...	4
NGC 3621	6.7 ± 0.5	65	0.83 ± 0.38	C	-3 ± 3	-17 ± 5	-0.47 ± 1.41	-2.11 ± 1.50	1
NGC 3627	10.6 ± 1.0	64	3.16 ± 1.46	A	$+9 \pm 4$...	$+1.33 \pm 0.74$...	1
NGC 3675	14.4 ± 3.1	67	1.00 ± 0.46	A	$+1 \pm 4$	$+1 \pm 3$	$+0.06 \pm 0.24$	$+0.04 \pm 0.23$	5
NGC 3898	22.1 ± 6.1	66	0.30 ± 0.14	A	$+8 \pm 3$	$+11 \pm 3$	$+1.31 \pm 0.87$	$+1.03 \pm 0.92$	4
NGC 3941	12.2 ± 1.7	50	0.03 ± 0.01	?	$+5 \pm 3$	$+6 \pm 4$	$+0.28 \pm 0.23$	$+0.17 \pm 0.15$	5
NGC 3992	17.1 ± 4.7	62	0.85 ± 0.39	A	-4 ± 3	$+0 \pm 4$	-0.76 ± 0.63	-0.31 ± 0.60	5
NGC 4192	16.8 ± 3.7	77	1.35 ± 0.62	A	$+0 \pm 3$	$+0 \pm 4$	-0.01 ± 0.51	$+0.06 \pm 0.59$	3
NGC 4258	7.6 ± 0.6	67	0.93 ± 0.43	A	-6 ± 3	-6 ± 4	-1.74 ± 1.08	-0.63 ± 0.52	2
NGC 4414	17.7 ± 1.8	56	2.88 ± 1.33	A	-11 ± 3	-12 ± 4	-1.03 ± 0.53	-1.05 ± 0.59	2
NGC 4535	15.8 ± 1.3	36	2.04 ± 0.94	A	-7 ± 4	...	-1.76 ± 1.22	...	3
NGC 4536	15.2 ± 1.9	66	2.95 ± 1.36	C	$+1 \pm 3$...	$+0.34 \pm 0.79$...	3
NGC 4548	16.2 ± 2.2	44	0.52 ± 0.24	C	-2 ± 5	-3 ± 4	-0.08 ± 0.29	-0.10 ± 0.21	3
NGC 4559	8.9 ± 0.8	66	0.66 ± 0.30	A	-4 ± 4	-2 ± 3	-0.86 ± 0.71	-0.20 ± 0.25	2
NGC 4651	16.8 ± 4.6	51	0.79 ± 0.37	A	-12 ± 3	...	-3.09 ± 1.50	...	3
NGC 4698	19.6 ± 4.2	70	0.15 ± 0.07	C	$+0 \pm 3$	$+1 \pm 4$	$+0.04 \pm 0.34$	$+0.02 \pm 0.34$	3
NGC 4725	12.4 ± 1.1	56	0.81 ± 0.37	C	$+7 \pm 3$...	$+1.21 \pm 0.89$...	4
NGC 4736	4.4 ± 0.4	40	0.47 ± 0.22	C	$+10 \pm 3$	$+19 \pm 3$	$+0.45 \pm 0.36$	$+0.76 \pm 0.80$	1
NGC 5005	18.4 ± 2.1	69	2.14 ± 0.99	A	$+7 \pm 3$	$+7 \pm 3$	$+0.35 \pm 0.31$	$+0.35 \pm 0.31$	5
NGC 5033	19.0 ± 2.7	66	2.88 ± 1.33	A	-7 ± 4	-7 ± 3	-3.33 ± 1.50	-1.58 ± 1.13	5
NGC 5055	8.9 ± 0.7	55	1.91 ± 0.88	C	$+0 \pm 3$	-1 ± 3	$+0.01 \pm 0.52$	-0.08 ± 0.43	2
NGC 5102	3.8 ± 0.3	71	0.01 ± 0.01	?	-4 ± 2	-5 ± 2	-0.08 ± 0.15	-0.09 ± 0.15	6
NGC 5161	25.5 ± 5.1	69	1.62 ± 0.75	A	$+5 \pm 3$	$+16 \pm 3$	$+0.91 \pm 1.50$	$+2.83 \pm 1.50$	7
NGC 5236	4.9 ± 0.5	40	4.17 ± 1.92	C	-7 ± 3	-1 ± 3	-1.73 ± 0.81	-0.01 ± 0.51	6
NGC 5350	30.9 ± 5.5	54	1.74 ± 0.80	C	-2 ± 3	-1 ± 3	-0.42 ± 0.52	-0.14 ± 0.26	8
NGC 5582	28.4 ± 3.9	53	0.04 ± 0.02	C	-1 ± 3	$+0 \pm 4$	-0.01 ± 0.54	-0.15 ± 0.52	8
NGC 6798	39.3 ± 10.5	62	0.11 ± 0.05	A	$+0 \pm 3$	$+0 \pm 3$	-0.01 ± 0.30	-0.00 ± 0.30	8
NGC 6946	7.7 ± 1.2	25	6.17 ± 2.84	C	-1 ± 3	-2 ± 3	-0.11 ± 0.68	-0.16 ± 0.75	1
NGC 7217	15.0 ± 4.1	34	0.62 ± 0.28	C	-1 ± 3	-3 ± 4	-0.05 ± 0.27	-0.12 ± 0.18	4
NGC 7331	14.7 ± 1.1	77	3.39 ± 1.56	C	-5 ± 3	-5 ± 3	-1.13 ± 1.50	-0.60 ± 1.50	1
NGC 7793	3.6 ± 0.3	46	0.25 ± 0.12	A	$+5 \pm 3$	$+4 \pm 3$	$+0.34 \pm 0.20$	$+0.10 \pm 0.15$	1
UGC 02080	14.4 ± 3.1	23	0.10 ± 0.05	A	-5 ± 3	...	-1.17 ± 0.98	...	4
UGC 02953	21.5 ± 3.9	49	0.60 ± 0.28	A	$+8 \pm 4$	$+9 \pm 4$	$+1.65 \pm 1.39$	$+1.74 \pm 1.42$	4

Appendix B Best-fit Parameters

In this appendix, we show plots of derived morphokinematical parameters for all 54 galaxies in our sample (Figure 7). Different rows indicate different galaxies. For each galaxy, we

plot the rotation curve (red circles) and the H I surface density (green triangles) in the left panel, the position angle (orange circles) and the inclination (blue triangles) in the middle panel, and the radial velocity (cyan circles) and mass flow rate (fuchsia triangles) in the right panel.

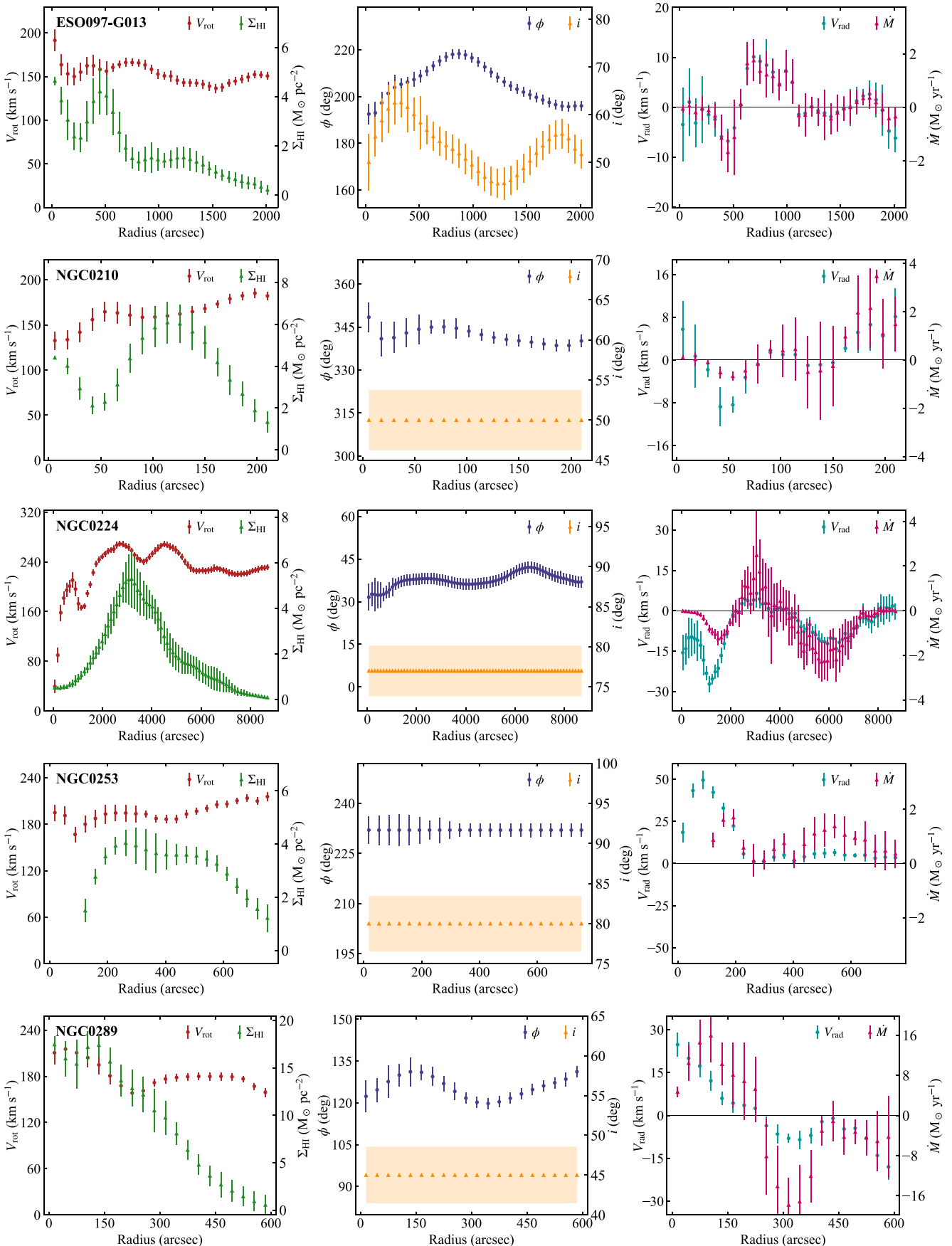


Figure 7. Kinematical parameters derived through 3D modeling.

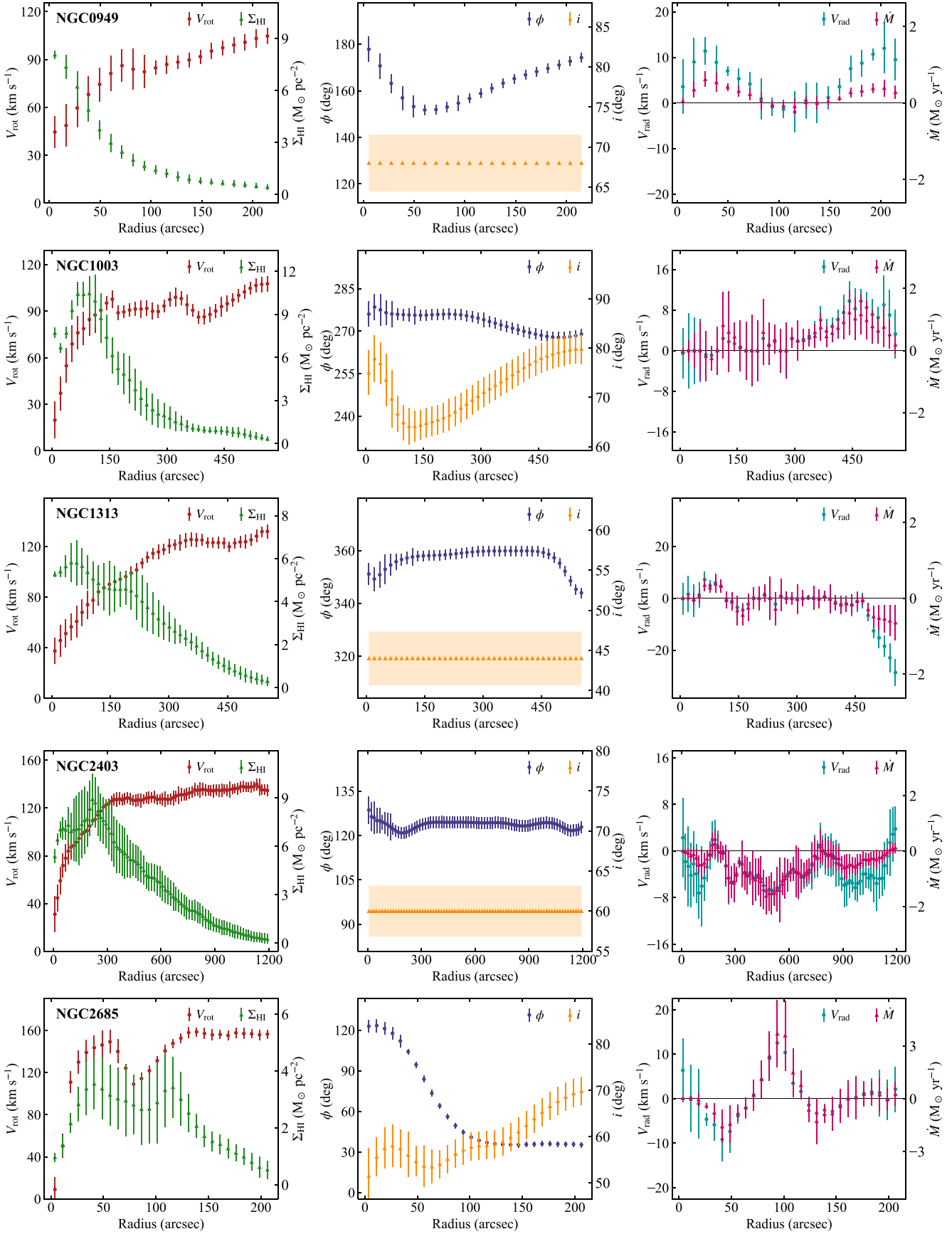


Figure 7. (Continued.)

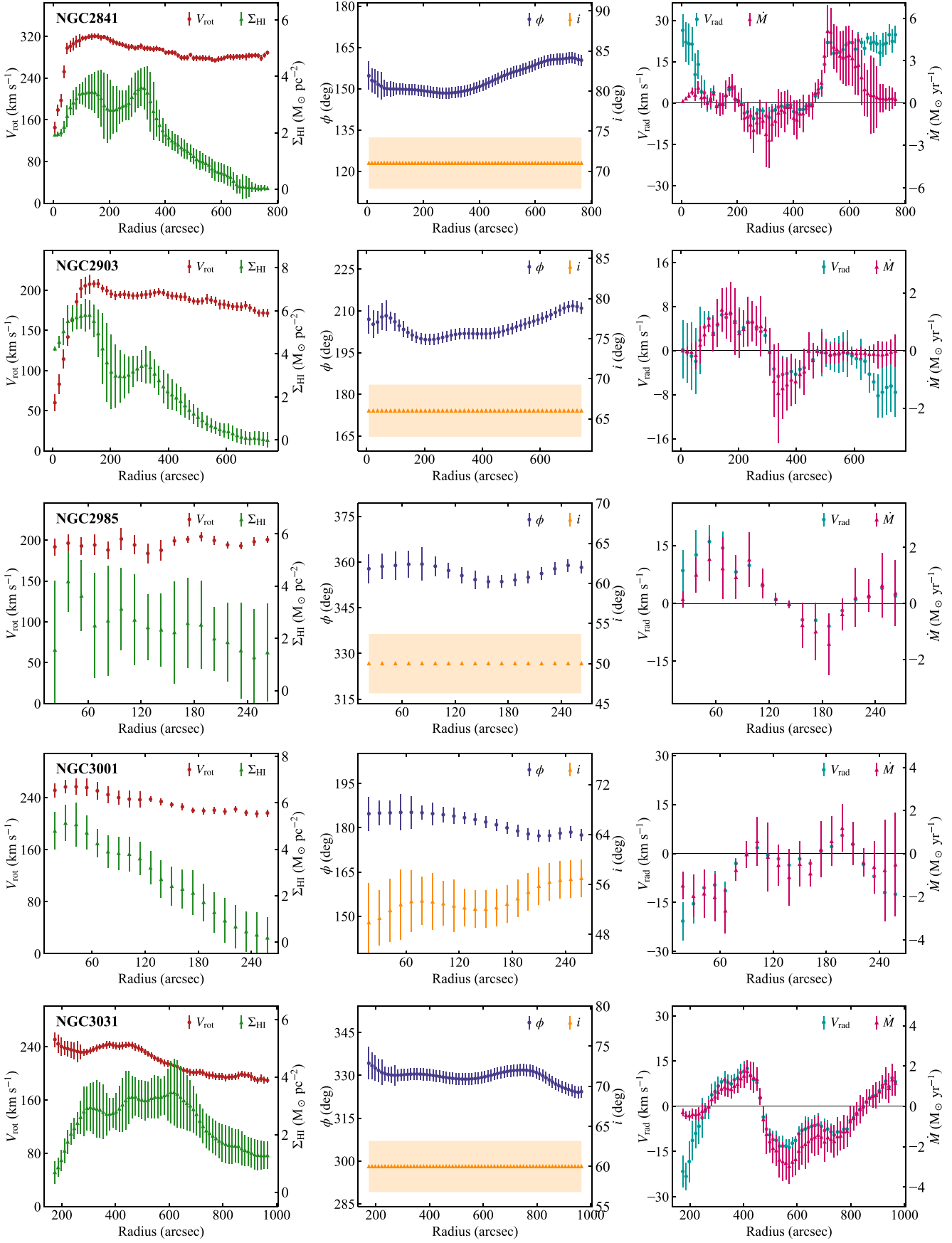


Figure 7. (Continued.)

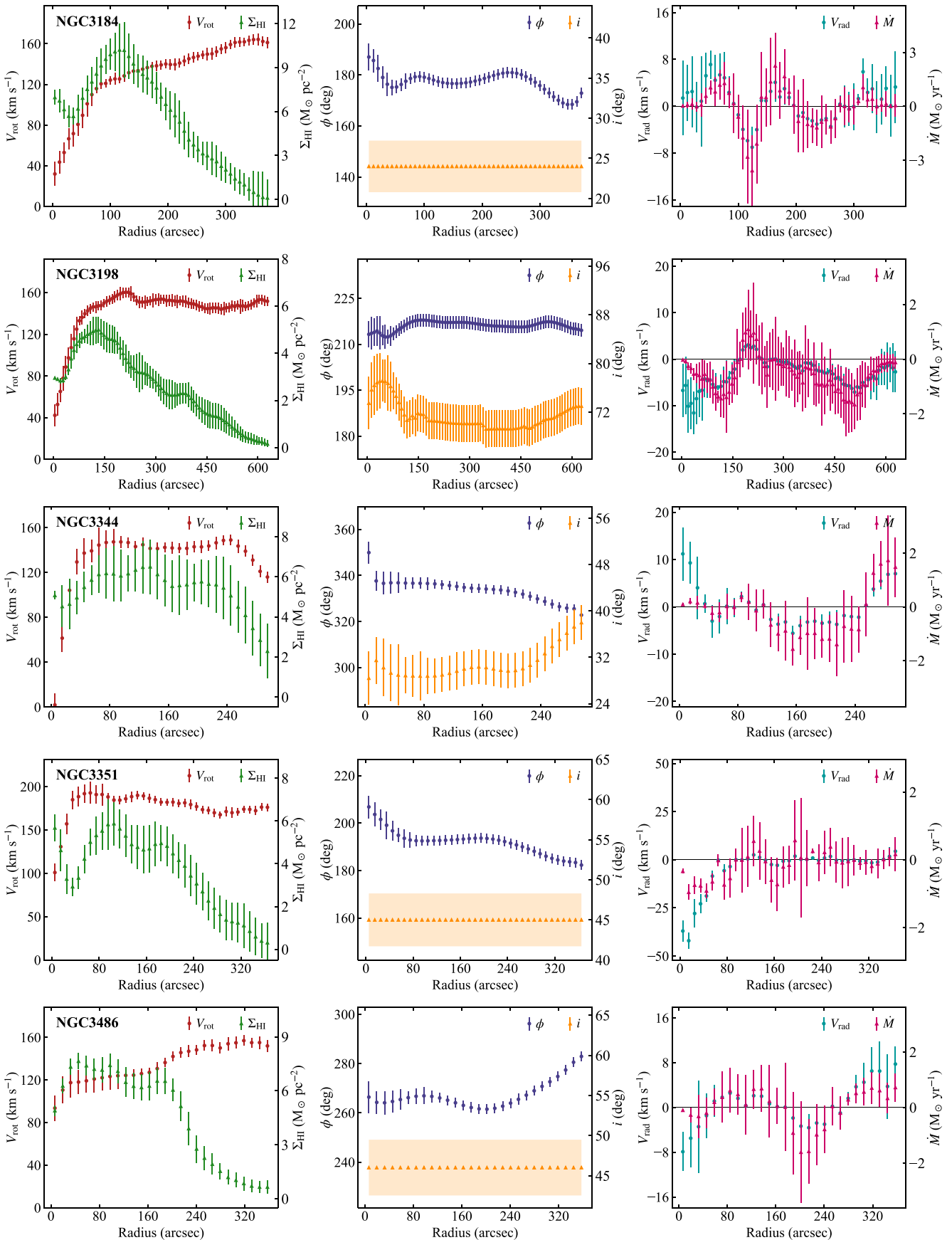


Figure 7. (Continued.)

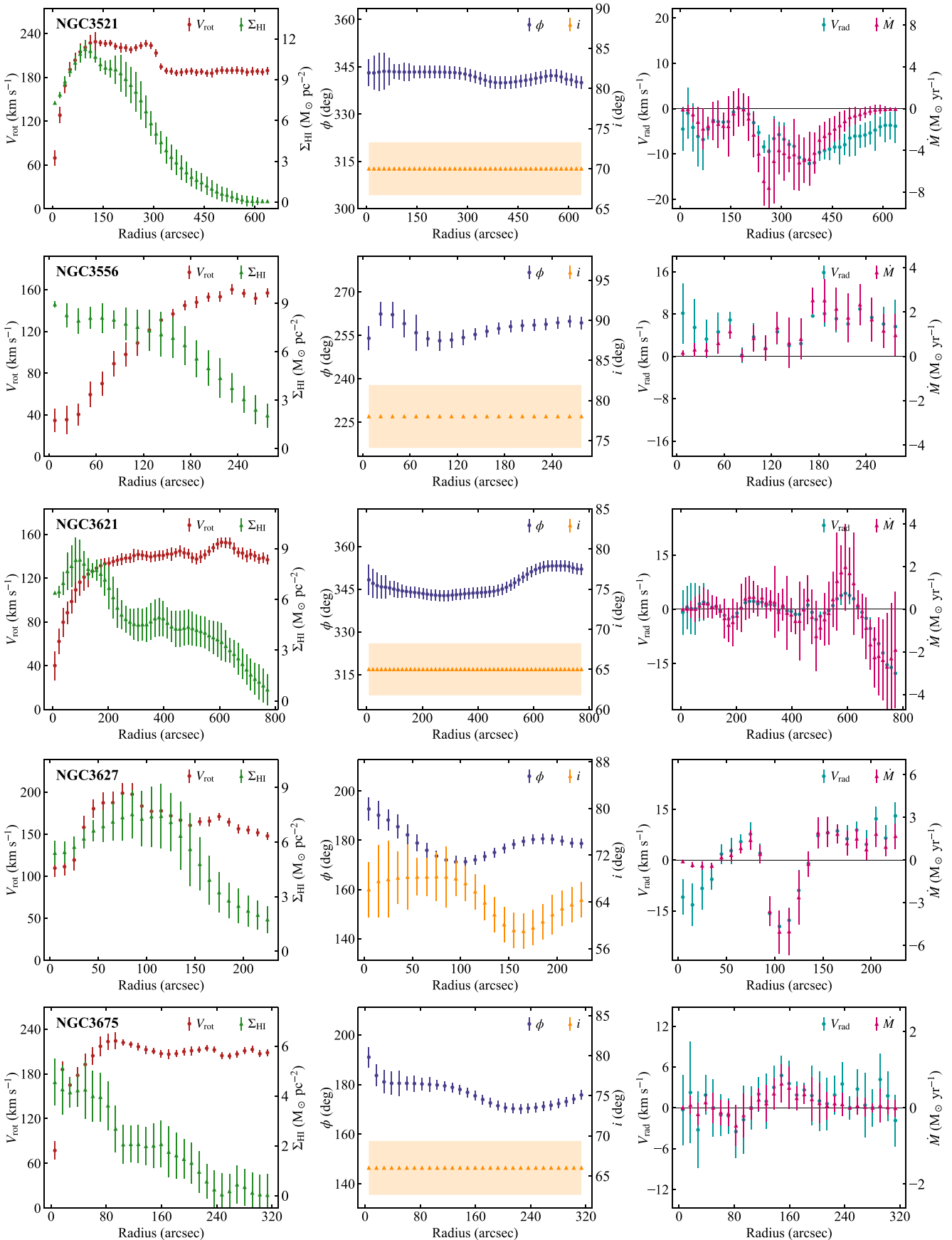


Figure 7. (Continued.)

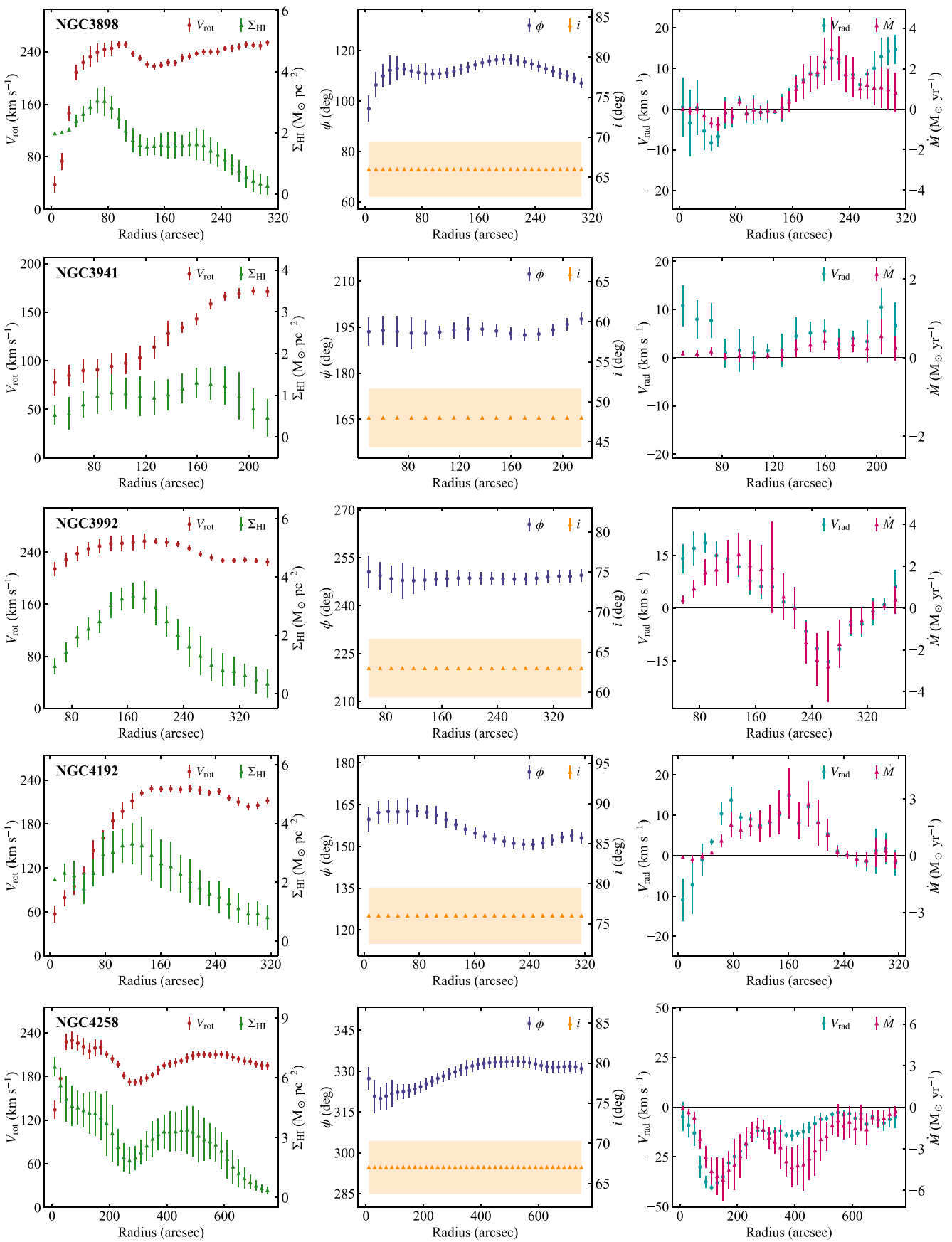


Figure 7. (Continued.)

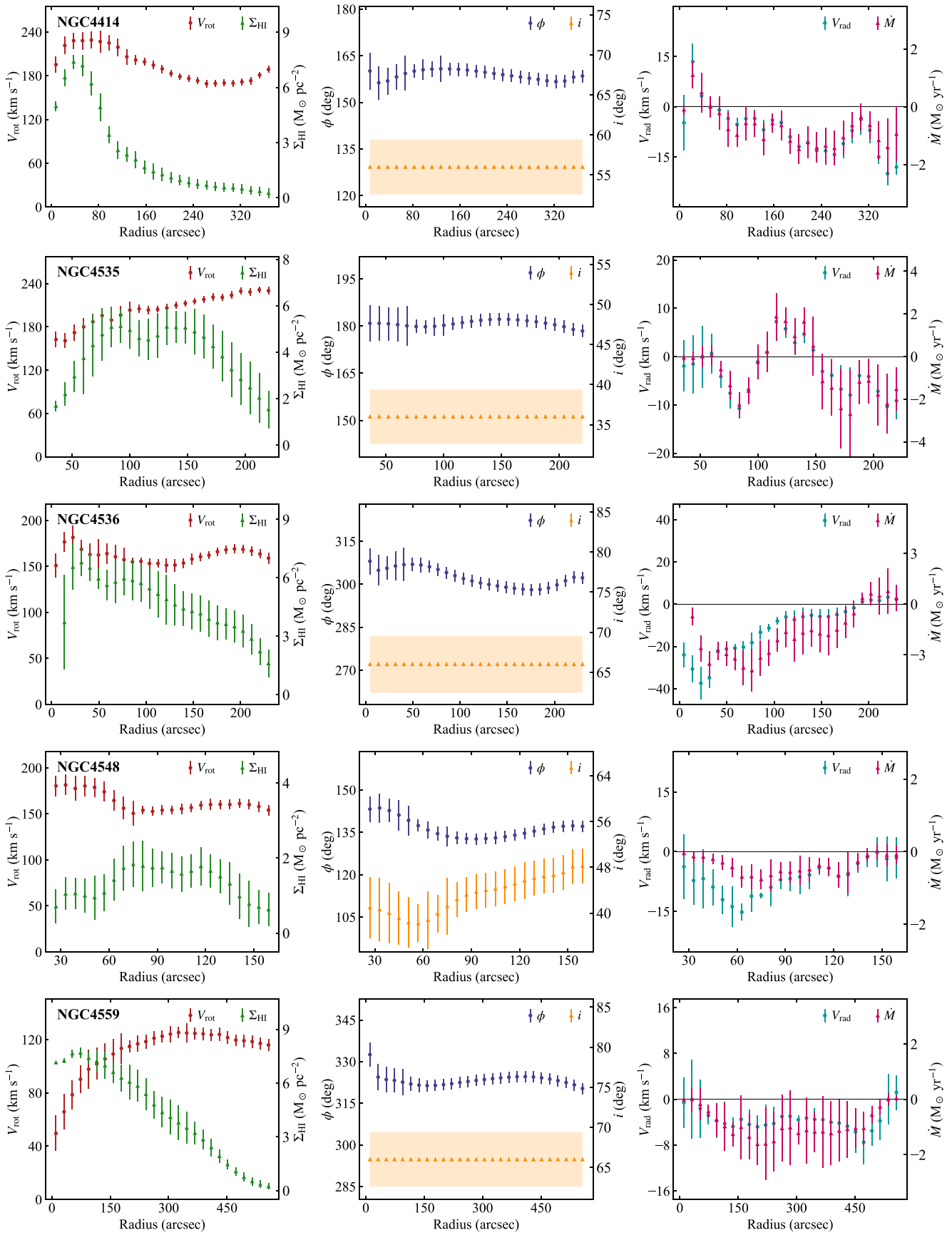


Figure 7. (Continued.)

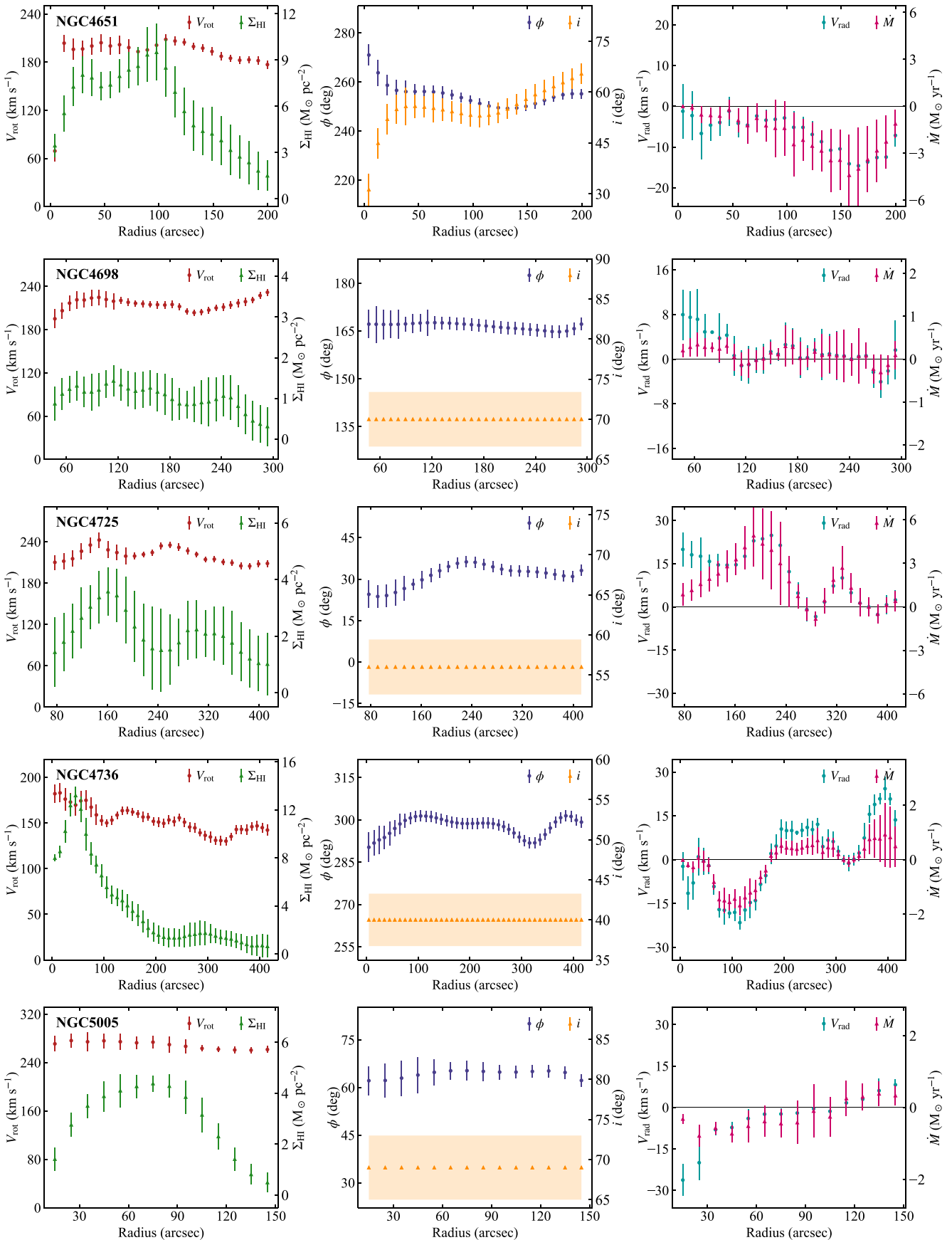


Figure 7. (Continued.)

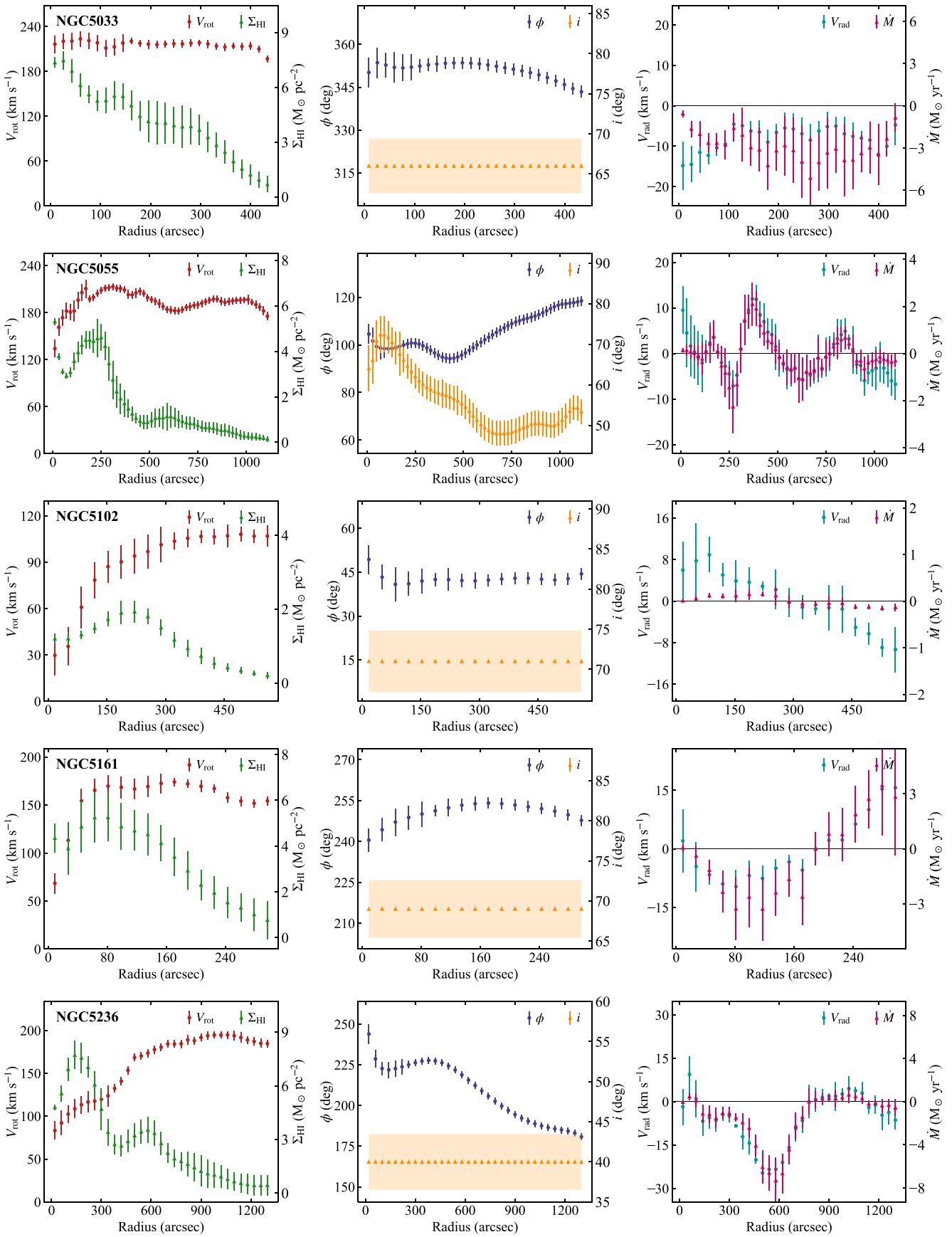


Figure 7. (Continued.)

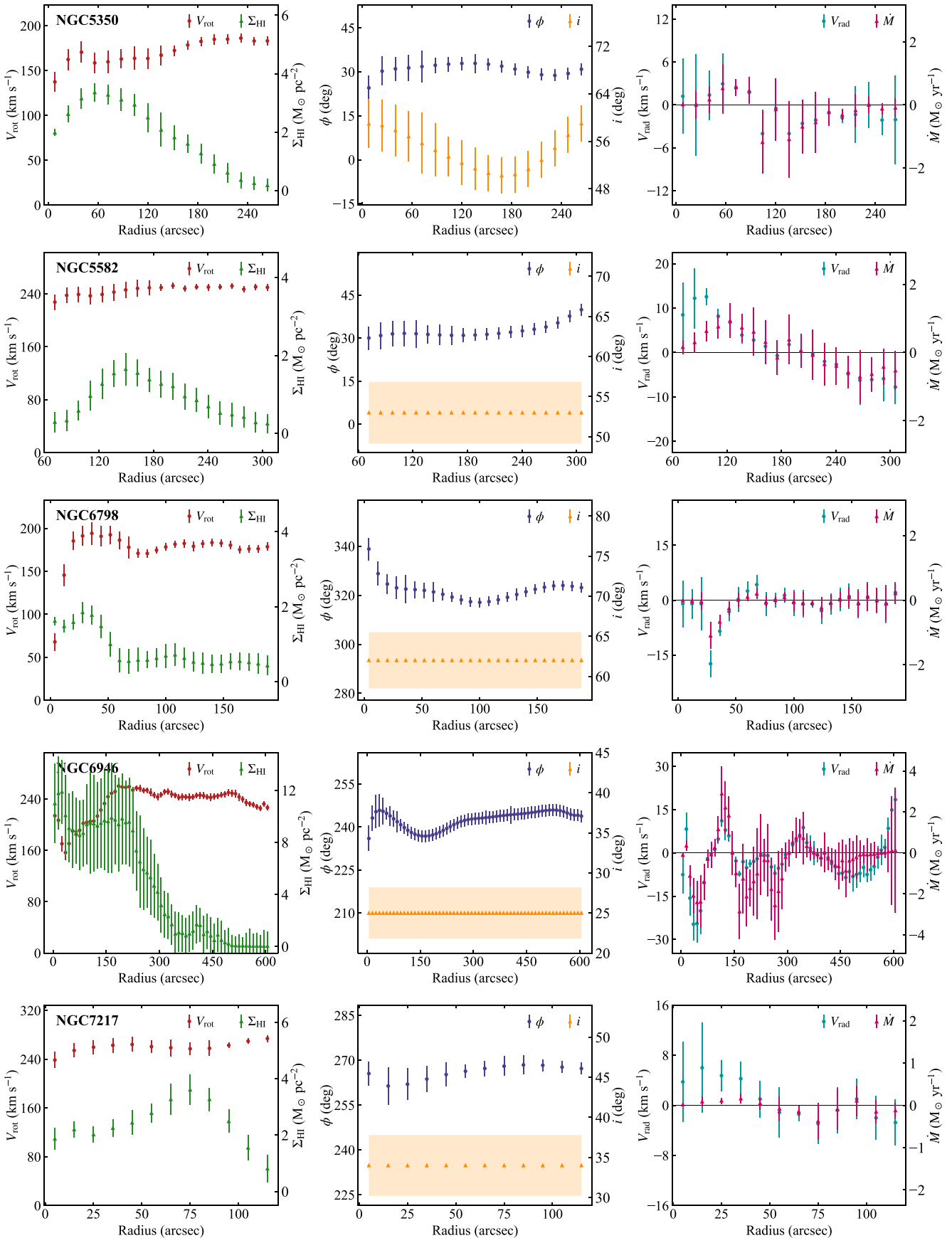


Figure 7. (Continued.)

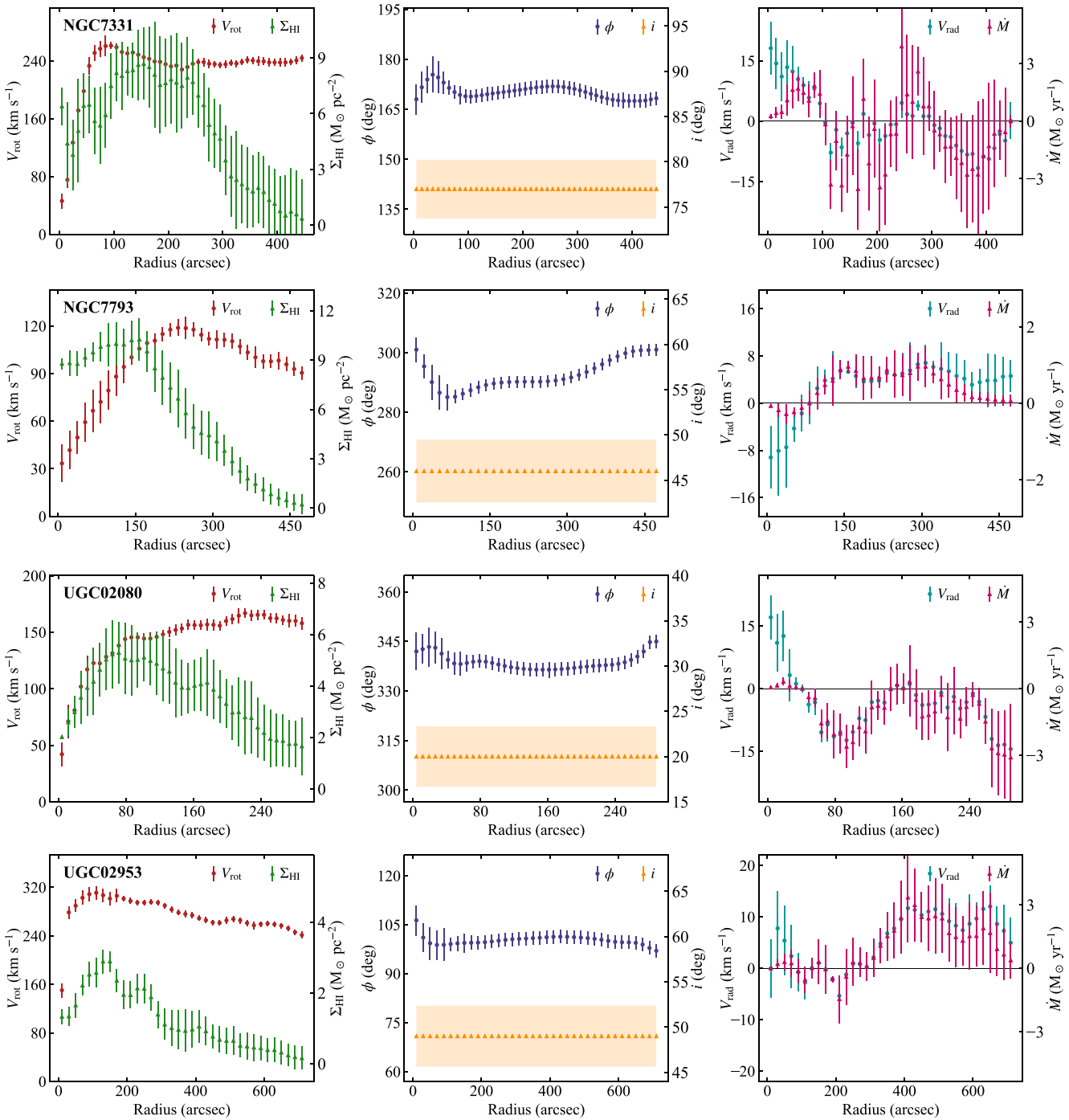


Figure 7. (Continued.)

ORCID iDs

Enrico M. Di Teodoro <https://orcid.org/0000-0003-4019-0673>
 J. E. G. Peek <https://orcid.org/0000-0003-4797-7030>

References

- Armillotta, L., Frernali, F., & Marinacci, F. 2016, *MNRAS*, **462**, 4157
 Armillotta, L., Krumholz, M. R., & Di Teodoro, E. M. 2020, *MNRAS*, **493**, 5273
 Armillotta, L., Krumholz, M. R., Di Teodoro, E. M., & McClure-Griffiths, N. M. 2019, *MNRAS*, **490**, 4401

Astropy Collaboration, Price-Whelan, A. M., Sipőcz, B. M., et al. 2018, *AJ*, **156**, 123

Aumer, M., & Binney, J. J. 2009, *MNRAS*, **397**, 1286

Battaglia, G., Frernali, F., Oosterloo, T., & Sancisi, R. 2006, *A&A*, **447**, 49

Begeman, K. G. 1987, PhD Thesis, Kapteyn Astronomical Institute, University of Groningen

Bigiel, F., Leroy, A. K., Walter, F., et al. 2011, *ApJL*, **730**, L13

Biliewski, T., & Schönrich, R. 2012, *MNRAS*, **426**, 2266

Braun, R., Thilker, D. A., Walterbos, R. A. M., & Corbelli, E. 2009, *ApJ*, **695**, 937

Briggs, D. S. 1995, PhD Thesis, The New Mexico Institute of Mining and Technology, <http://www.aoc.nrao.edu/dissertations/dbriggs>

Chambers, K. C., Magnier, E. A., Metcalfe, N., et al. 2016, arXiv:1612.05560

- Chung, A., van Gorkom, J. H., Kenney, J. D. P., Crowl, H., & Vollmer, B. 2009, *AJ*, **138**, 1741
- Cluver, M. E., Jarrett, T. H., Dale, D. A., et al. 2017, *ApJ*, **850**, 68
- Dey, A., Schlegel, D. J., Lang, D., et al. 2019, *AJ*, **157**, 168
- Di Teodoro, E. 2021, 3D-Barolo: Kinematic Modelling of Emission-line Data, 1.6.1, Zenodo, doi:[10.5281/zenodo.5510565](https://doi.org/10.5281/zenodo.5510565)
- Di Teodoro, E. M., & Frernali, F. 2014, *A&A*, **567**, A68
- Di Teodoro, E. M., & Frernali, F. 2015, *MNRAS*, **451**, 3021
- Eisenstein, D. J., Weinberg, D. H., Agol, E., et al. 2011, *AJ*, **142**, 72
- El-Badry, K., Quataert, E., Wetzel, A., et al. 2018, *MNRAS*, **473**, 1930
- Fall, S. M., & Efstathiou, G. 1980, *MNRAS*, **193**, 189
- Frernali, F., & Tomassetti, M. 2012, *MNRAS*, **426**, 2166
- Goetz, M., & Koeppen, J. 1992, *A&A*, **262**, 455
- Haywood, M., Snaith, O., Lehnert, M. D., Di Matteo, P., & Khoperskov, S. 2019, *A&A*, **625**, A105
- Heald, G., Józsa, G., Serra, P., et al. 2011, *A&A*, **526**, A118
- Ho, S. H., Martin, C. L., Kacprzak, G. G., & Churchill, C. W. 2017, *ApJ*, **835**, 267
- Ho, S. H., Martin, C. L., & Turner, M. L. 2019, *ApJ*, **875**, 54
- Kalberla, P. M. W., & Dedes, L. 2008, *A&A*, **487**, 951
- Kereš, D., Katz, N., Weinberg, D. H., & Davé, R. 2005, *MNRAS*, **363**, 2
- Kerp, J., Kalberla, P. M. W., Ben Bekhti, N., et al. 2016, *A&A*, **589**, A120
- Koribalski, B. S., Wang, J., Kamphuis, P., et al. 2018, *MNRAS*, **478**, 1611
- Lacey, C. G., & Fall, S. M. 1985, *ApJ*, **290**, 154
- Lagos, C. d. P., Theuns, T., Stevens, A. R. H., et al. 2017, *MNRAS*, **464**, 3850
- Leroy, A. K., Sandstrom, K. M., Lang, D., et al. 2019, *ApJS*, **244**, 24
- Leroy, A. K., Walter, F., Brinks, E., et al. 2008, *AJ*, **136**, 2782
- Lutz, K. A., Kilborn, V. A., Catinella, B., et al. 2017, *MNRAS*, **467**, 1083
- Madau, P., & Dickinson, M. 2014, *ARA&A*, **52**, 415
- Marinacci, F., Binney, J., Frernali, F., et al. 2010, *MNRAS*, **404**, 1464
- Martin, D. C., Fanson, J., Schiminovich, D., et al. 2005, *ApJL*, **619**, L1
- Martinez-Medina, L. A., Pichardo, B., & Peimbert, A. 2020, *MNRAS*, **496**, 1845
- Mott, A., Spitoni, E., & Matteucci, F. 2013, *MNRAS*, **435**, 2918
- Nelson, D., Vogelsberger, M., Genel, S., et al. 2013, *MNRAS*, **429**, 3353
- Nuza, S. E., Scannapieco, C., Chiappini, C., et al. 2019, *MNRAS*, **482**, 3089
- Okalidis, P., Grand, R. J. J., Yates, R. M., & Kauffmann, G. 2021, *MNRAS*, **504**, 4400
- Panter, B., Jimenez, R., Heavens, A. F., & Charlot, S. 2007, *MNRAS*, **378**, 1550
- Pezzulli, G., & Frernali, F. 2016, *MNRAS*, **455**, 2308
- Pichon, C., Pogosyan, D., Kimm, T., et al. 2011, *MNRAS*, **418**, 2493
- Portinari, L., & Chiosi, C. 2000, *A&A*, **355**, 929
- Putman, M. E., Peek, J. E. G., & Joung, M. R. 2012, *ARA&A*, **50**, 491
- Raba, R., Schiebel, D., Emonts, B., et al. 2020, Astronomical Data Analysis Software and Systems (ADASS) XXIX, in ASP Conf. Ser. 527 ed. R. Pizzo et al. (San Francisco, CA: Astronomical Society of the Pacific), 271
- Richards, E. E., van Zee, L., Barnes, K. L., et al. 2016, *MNRAS*, **460**, 689
- Roberts, M. S. 1975, in Radio Observations of Neutral Hydrogen in Galaxies, ed. A. Sandage, M. Sandage, & J. Kristian (Chicago, IL: Univ. Chicago Press), 309
- Sancisi, R., Frernali, F., Oosterloo, T., & van der Hulst, T. 2008, *A&ARv*, **15**, 189
- Schmidt, T. M., Bigiel, F., Klessen, R. S., & de Blok, W. J. G. 2016, *MNRAS*, **457**, 2642
- Serra, P., Oosterloo, T., Morganti, R., et al. 2012, *MNRAS*, **422**, 1835
- Spekkens, K., & Sellwood, J. A. 2007, *ApJ*, **664**, 204
- Stern, J., Fielding, D., Faucher-Giguère, C.-A., & Quataert, E. 2020, *MNRAS*, **492**, 6042
- Stewart, K. R., Brooks, A. M., Bullock, J. S., et al. 2013, *ApJ*, **769**, 74
- Stewart, K. R., Kaufmann, T., Bullock, J. S., et al. 2011, *ApJ*, **738**, 39
- Thon, R., & Meusinger, H. 1998, *A&A*, **338**, 413
- Trachternach, C., de Blok, W. J. G., Walter, F., Brinks, E., & Kennicutt, R. C. J. 2008, *AJ*, **136**, 2720
- Trapp, C., Keres, D., Chan, T. K., et al. 2021, arXiv:[2105.11472](https://arxiv.org/abs/2105.11472)
- Tully, R. B., Courtois, H. M., & Sorce, J. G. 2016, *AJ*, **152**, 50
- Tully, R. B., Rizzi, L., Shaya, E. J., et al. 2009, *AJ*, **138**, 323
- Tumlinson, J., Peebles, M. S., & Werk, J. K. 2017, *ARA&A*, **55**, 389
- van den Bergh, S. 1962, *AJ*, **67**, 486
- van der Hulst, J. M., van Albada, T. S., & Sancisi, R. 2001, in ASP Conf. Ser. 240, Gas and Galaxy Evolution, ed. J. E. Hibbard, M. Rupen, & J. H. van Gorkom (San Francisco, CA: ASP), 451
- Wakker, B. P., & van Woerden, H. 1997, *ARA&A*, **35**, 217
- Walter, F., Brinks, E., de Blok, W. J. G., et al. 2008, *AJ*, **136**, 2563
- Westmeier, T., Braun, R., & Thilker, D. 2005, *A&A*, **436**, 101
- Wong, T., Blitz, L., & Bosma, A. 2004, *ApJ*, **605**, 183
- Worley, G., Dorman, B., & Jones, L. A. 1996, *AJ*, **112**, 948
- Wright, E. L., Eisenhardt, P. R. M., Mainzer, A. K., et al. 2010, *AJ*, **140**, 1868